SITE INVESTIGATION, AND GIS AND SLOPE STABILITY ANALYSIS OF A FROZEN DEBRIS LOBE, SOUTH-CENTRAL BROOKS RANGE, ALASKA

By

Jocelyn M. Simpson

RECOMMENDED:

Dr. Scott L. Huang

Dr. Ronald P. Daanen

Dr. Trent D. Hubbard

Dr. Margaret M. Darrow
Advisory Committee Chair

Dr. Margaret M. Darrow
Chair, Department of Mining and Geological Engineering

APPROVED:

Dr. Douglas J. Goering
Dean, College of Engineering and Mines

Dr. John C. Eichelberger
Dean of the Graduate School

11 August 2015
Date

SITE INVESTIGATION, AND GIS AND SLOPE STABILITY ANALYSIS OF A FROZEN DEBRIS LOBE, SOUTH-CENTRAL BROOKS RANGE, ALASKA

A

THESIS

Presented to the Faculty

of the University of Alaska Fairbanks

in Partial Fulfillment of the Requirements

for the Degree of

MASTER OF SCIENCE

By

Jocelyn Simpson, B.S.

Fairbanks, AK

August 2015

ABSTRACT

Frozen debris lobes (FDLs) are large masses of soil, rock, incorporated organic material, and ice moving down permafrost-affected slopes in the south-central Brooks Range, Alaska. Here we focus on FDL-A, which is an impending geohazard to the Dalton Highway, located just under 40 m away from the embankment. We present the results of multi-faceted research, including field-based studies, GIS analysis, laboratory testing of soil samples, and slope stability analysis. Subsurface instrumentation indicates that major movement of FDL-A occurs in a shear zone 20.6 to 22.8 m below the ground surface, with temperature-dependent internal flow as a secondary movement mechanism. Field observations indicate the presence of massive, infiltration ice associated with cracks on the surface of the lobe. Surface measurements show an overall average rate of movement of 1.2 cm per day, which is an increase over historic rates. The GIS analysis also provided insight into the movement and instability of FDL-A, and provided groundwork for a GIS protocol to examine catchment and lobe features of all FDLs along the highway corridor. The slope stability analysis required a back analysis to determine soil strength parameters at failure, resulting in cohesion values between 43 to 53 kPa and friction angles between 10° and 16°. The modeling results indicated a high sensitivity to cohesion and pore water pressure. This is critical since the melting of massive ice and thawing of frozen soil will increase pore water pressure and lower shear strength, resulting in the acceleration of FDL-A towards the Dalton Highway.

TABLE OF CONTENTS

Page

Page

LIST OF FIGURES

Page

LIST OF TABLES

Page

LIST OF APPENDICES

Page

ACKNOWLEDGEMENTS

I would first like to express my appreciation to my advisor, Dr. Margaret Darrow. Her guidance, encouragement, knowledge, and expertise have been priceless during my educational endeavors. Dr. Darrow's dedication to exceptional instruction and her patience during the course of this research have made this a positive and motivating experience for me.

Additionally, I would like to thank the rest of my graduate committee members, Dr. Scott Huang, Dr. Ronald Daanen, and Dr. Trent Hubbard. Their knowledge and advice have been extremely valuable.

I would also like to thank my family. My parents, Anthony and Jacqueline Jerome, have always been supportive and encouraging. Most of all, I would like to thank my husband Mark, who has always stood beside me with confidence and has been a source of inspiration to work hard and do my best.

This research was funded by grants from the US Department of Transportation (DTRT06-G-0011), the Alaska Department of Transportation and Public Facilities (T2-12-17), and through generous support from the Alaska Division of Geological & Geophysical Surveys' Capital Improvements Project, and the Alyeska Pipeline Service Company.

CHAPTER 1 INTRODUCTION

Along the Dalton Highway corridor, in the south-central Brooks Range, Alaska, large masses of frozen debris are moving down permafrost-affected slopes. These features, named frozen debris lobes (FDLs), are located in a region that is characterized by steep terrain, active slope processes, and continuous permafrost. FDLs consist of soil, rock, incorporated organic material, and ice, and with their recent increasing rate of movement, they have the potential to threaten the Dalton Highway and the Trans Alaska Pipeline System (TAPS) within the corridor. We identified more than 40 FDLs along the highway corridor between milepost (MP) 194 and MP 230, selecting eight FDLs due to their proximity to infrastructure for further examination, including field investigations and remote sensing analysis. While our focus has been on FDLs within the highway corridor, examination of available imagery has proven that many FDL-like features are present throughout the Brooks Range. One of these lobes, FDL-A, is just under 40 m from the highway and has been the main focus of FDL research since 2008 (see Figure 1.1). Recent data indicates that FDL-A's rate of movement has been increasing (Daanen et al., 2012) and ongoing research has helped us better understand this feature.

1.1 Background

Snow, glaciers, and permafrost in cold mountain areas are sensitive to changes in atmospheric conditions, and mass wasting often occurs in mountain areas with steep slopes due to changes in geomorphic processes (Haeberli and Beniston, 1998). The stability of permafrost terrain is vulnerable to thermal changes as thawing reduces the strength of frozen soil and fractured bedrock. Ice-rich soils undergo thaw consolidation and experience an increase in pore water pressure, which then leads to increased instability (Harris, 2005). In areas with steep

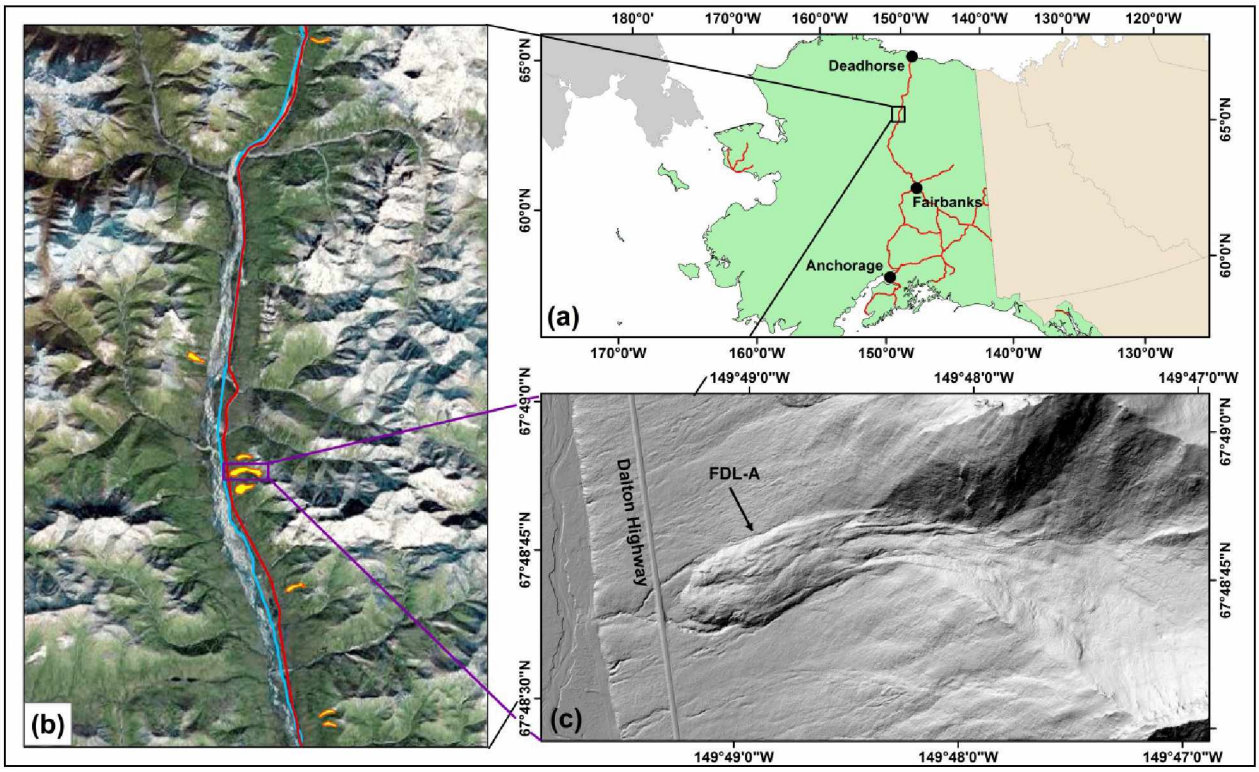

Figure 1.1. Location of FDL study area. In (a) the study area (indicated by the black rectangle) is shown relative to select populated locations and major road systems in Alaska; (b) depicts the eight FDLs selected for further analysis (shown in yellow), the Dalton Highway (shown in red), and TAPS (shown in blue); and (c) is a large-scale view of FDL-A. (Base map data from Esri (2015) and Hubbard et al. (2011)).

mountainous terrain and thawing of soil and rocks, this instability can result in debris flows, landslides, deep-seated bedrock failures, rock slides, rock falls, creep-related processes, and active layer detachment failures (Kääb et al., 2005; Harris et al., 2001).

Many types of mass movement related to degrading permafrost have been studied in parts of Europe and Canada. Shallow landslides, mud and debris flows, and rock falls are commonly seen in high mountain areas of Europe (Harris and Vonder Mühll, 2001), and active layer detachments and debris flows have been observed in Yukon Territory, Canada (Harris and Lewkowicz, 2000; Huscroft et al., 2003). Debris flows researched in Europe are frequently initiated as translational slides over the permafrost table, developing into debris flows as water contents and slope gradients increase (Harris et al., 2009). In Canada, active layer detachment slides can result from rapid thawing at the base of the active layer and are usually triggered by forest fires (Lipovsky and Huscroft, 2006). Debris flows and landslides observed in the Yukon Territory occur where thawing takes place in ice-rich soils, resulting in a great reduction in volume and strength (Huscroft et al., 2003). Another common type of slope movement seen in these areas, as well as in Alaska, is solifluction, which is a slow downslope movement of saturated soil by frost creep, needle ice creep, or gelifluction, and is caused by poor drainage of pore water and freezing during the winter months (Tart, Jr., 1996; Davis, 2001; Harris and Lewkowicz, 2000; Matsuoka, 2001; Matsuoka, 2014). As the soil thaws in the spring it becomes saturated and slowly creeps down slope. As the upper layer thaws and drains, it becomes more stable but still moves on top of ice-rich materials. This movement eventually stops when the ground refreezes (Tart, Jr., 1996).

Rock glaciers are a common permafrost-related movement feature in mountainous areas and are found in many major mountain systems (Davis, 2001). Rock glaciers are described as

lobate or tongue-shaped masses forming at the base of cliffs and talus slopes or extending from the end of small glaciers. In Alaska, Wahrhaftig and Cox (1959) investigated rock glaciers in the Alaska Range and found they consisted of a layer of coarse block rubble overlaying a thicker, layer of coarse blocks mixed with sand and silt material. The ice in these rock glaciers originated from compacted snow, melting snow or rain, or groundwater that rose beneath the talus and froze upon contact with cold air. Active rock glaciers were found to be almost entirely rock debris mixed with ice accounting for approximately one-half of a typical rock glacier's volume, and their movement resulted from deformation of the interstitial ice (Wahrhaftig and Cox, 1959; Davis, 2001). The slope-dependent movement rates of rock glaciers are typically up to 1 m per year; however, in warm alpine settings this rate could be higher (Davis, 2001; Barboux et al., 2014). Four major rock types that form blocky and boulder-like debris found in rock glaciers are granite, gneiss, sandstone, and limestone, while platy rock and micaceous schists are unfavorable to rock glacier formation (Wahrhaftig and Cox, 1959; Haeberli et al., 2006).

As part of the continuum of slope movement processes, frozen debris lobes were originally identified as flow slide deposits exhibiting slow downslope movement (Hamilton, 1978; 1979; 1981). They were later described mostly as inactive rock glaciers (Kreig and Reger, 1982; Brown and Kreig, 1983); however, on-going research has shown they differ from rock glaciers with respect to source, composition, rate, and mechanism of movement. These features were "rediscovered" in 2008 and preliminary studies, mainly on FDL-A, identified indicators of on-going movement such as leaning and split trees, overrun and buried trees, over-steepened slopes, frozen blocks showing slickens from sliding, and uplifting of frozen topsoil in front of the lobe (Daanen et al., 2012). Remote sensing analysis carried out by Daanen et al. (2012) revealed that the rate of movement for FDL-A increased between 1955 and 2008, with rates increasing

from 0.58 to approximately 1 cm per day. While these studies were preliminary, they provided insight into the growing hazards of slope instability and mass movement in areas where permafrost warming and degradation is occurring.

Through several years of field monitoring we have observed evidence of movement and geomorphic characteristics of FDL-A. Investigation of the catchment, the area upslope of the lobe that serves as its debris source, indicates that weak and platy bedrock moving downslope mainly through solifluction and rock falls (see Figure 1.2) is the source of debris for FDL-A (Daanen et al., 2012; Spangler et al., 2013). As FDL-A continues to move downhill, evidence of its movement is ubiquitous across its surface in many forms including longitudinal cracks (see Figure 1.3a). Trees that lean with ongoing near-surface movement and prolific splitting of trunks are evidence of tension at the surface (see Figure 1.3b). Trees and shrubs also are knocked down and buried at the toe of the lobe (see Figure 1.3d). Shear at the toe is most easily observed during the winter as the frozen, rigid lobe moves over undisturbed ground leaving a void space underneath that collapses the following summer (see Figure 1.3c).

In 2009, we observed that the main drainage on the surface of FDL-A shifted from its original channel into a new channel draining to the southwest and over the left flank (see Figure 1.4). This resulted in significant erosion of that portion of the left flank. The creek moved back to its original channel in June 2014, but bifurcated in August of that same year, flowing in both channels. As a result of the channel movement, there was an increase in longitudinal cracking and destabilization of the forest near the left flank of FDL-A (Darrow et al., 2015).

The summer of 2014 was the wettest on record for parts of Interior Alaska, and significant rainfall caused appreciable changes in FDL-A. Perhaps the most dramatic changes

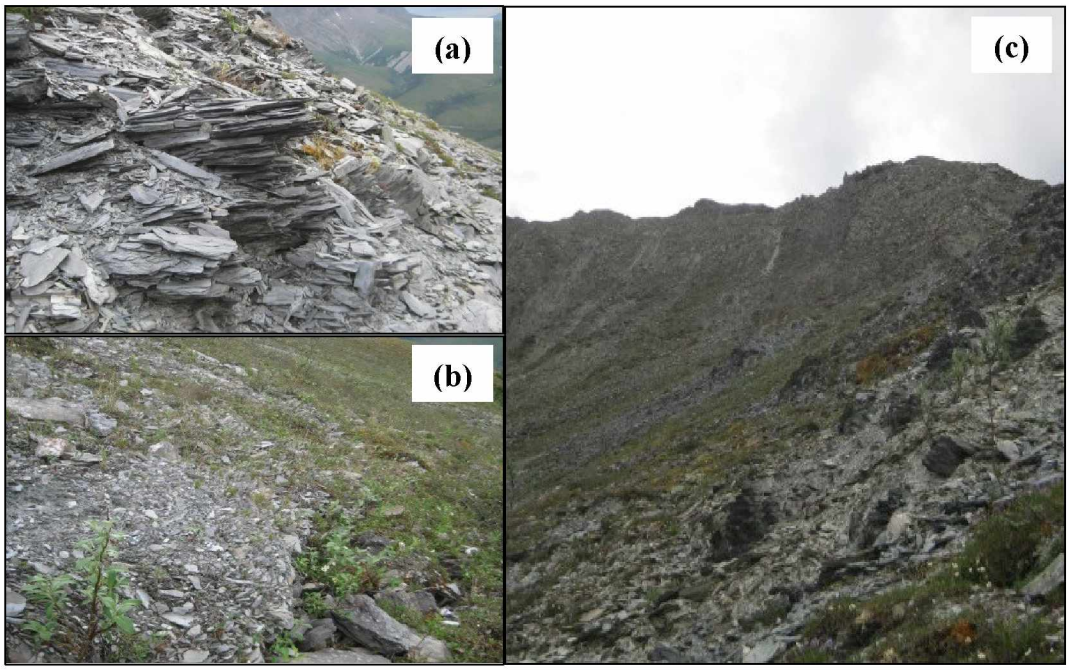

Figure 1.2. Bedrock and slope processes in the catchment of FDL-A. Weak, platy bedrock, such as the phyllite in (a), is typically found in this area. Solifluction shown in (b) carries rock and soil through the catchment and will eventually contribute to the debris forming FDL-A. Rock fall contributes to FDL-A along the steep ridge line (c) that makes up the southern boundary of the catchment.

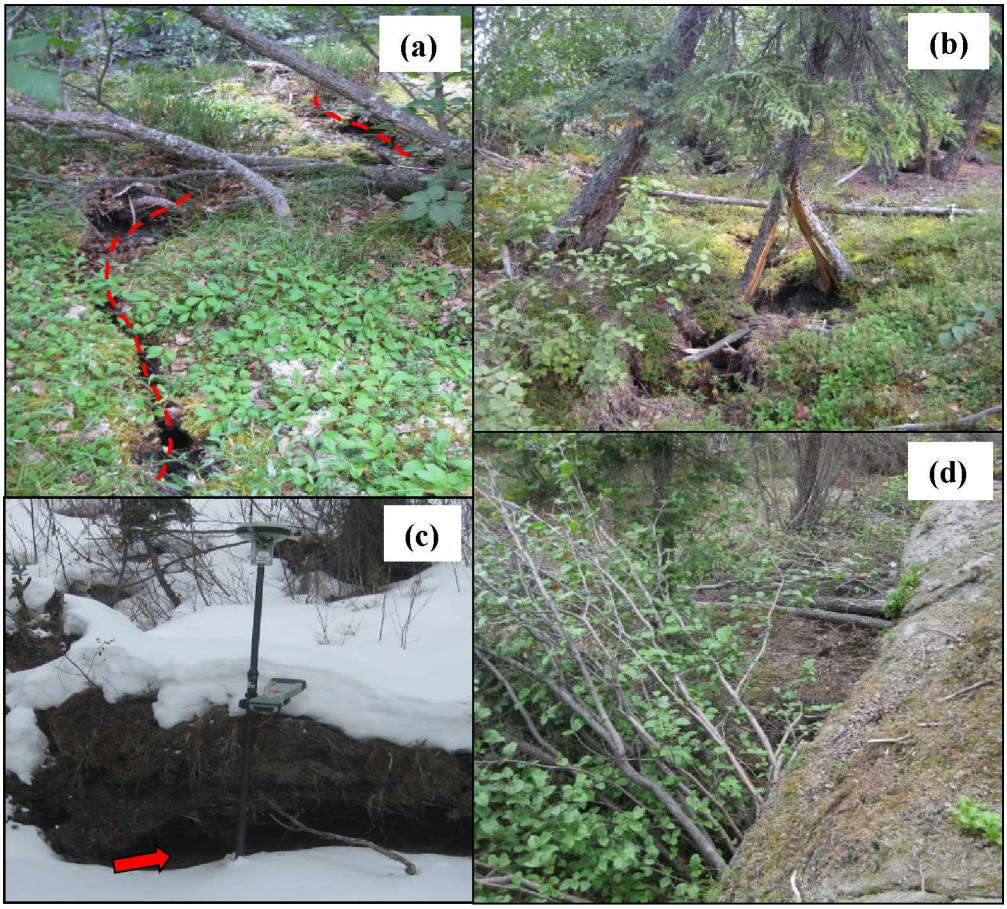

Figure 1.3. Evidence of ongoing movement of FDL-A. (a) Longitudinal crack (dashed red line) among leaning and falling trees; (b) split and leaning trees near the left flank; (c) a void (indicated by the red arrow) under the toe of FDL-A as it shears over undisturbed ground; (d) trees knocked over, buried, and incorporated into FDL-A at the toe.

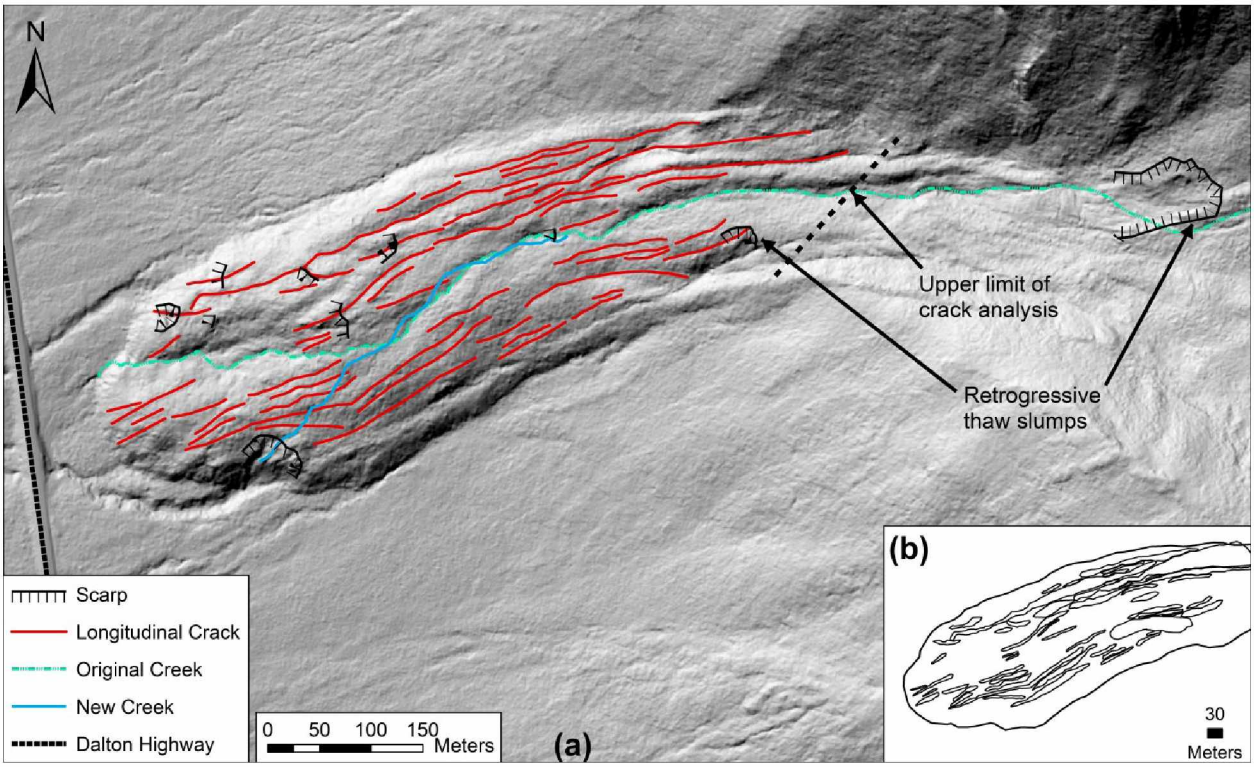

Figure 1.4. FDL-A surface features. (a) Scarps, longitudinal cracks, and creeks, including the location of two Retrogressive Thaw Slumps (RTS); (b) outline of FDL-A and major longitudinal cracks. (Base map from 2011 LiDAR image (Hubbard et al., 2011)).

occurred in two retrogressive thaw slumps (RTS), a lower RTS near the left flank and a higher RTS in the catchment area (see Figure 1.4). The significant rainfall exposed massive ice in the head scarps of both of these areas. Based on field observations, we developed a working hypothesis for the formation of this ice, and collected water and ice samples for isotope analysis; the results of this analysis and our working hypothesis will be discussed below.

1.2 Objectives

The objectives of this study are to present the results of:

1) field-based studies, including data from drilling and instrumentation, surface measurements made using a differential global positioning system (DGPS), and observations from several years of on-going monitoring;

2) a GIS analysis of the lobe and its catchment;

3) laboratory testing of soil samples to determine strength parameters; and

4) a slope stability analysis using a limit equilibrium approach.

We use these results to determine the mechanisms of movement and movement rate of FDL-A and its defining characteristics in order to understand these landslides in frozen soil and to predict their response to varying parameters such as changes in climate.

This thesis has been modified from a document originally written for and submitted to the *Environmental and Engineering Geoscience* journal, with coauthors Margaret M. Darrow, Scott L. Huang, Ronald P. Daanen, and Trent D. Hubbard. While the focus of this thesis is work on FDL-A, seven other FDLs were investigated in the field. This thesis contains the results of grain

size analysis (see Appendix A) and strength testing results of rock samples (see Appendix B) collected from all of the FDLs under investigation.

CHAPTER 2 METHODS

2.1 Field Studies

2.1.1 Subsurface Investigation

The focus of our research has been FDL-A due to the imminent threat it presents to the Dalton Highway, the main transportation route between Interior Alaska and the North Slope (see Figure 1.1). During September 2012, we worked with Alaska Department of Transportation and Public Facilities (ADOT&PF) personnel to conduct a drilling program on FDL-A to: 1) obtain soil samples for laboratory testing; 2) determine the thickness and composition of the lobe; and 3) install instruments to measure slope movement, temperature, and water pressure. A total of six boreholes were drilled, three on and three immediately adjacent to the lobe to the south and west. All sampled soils were classified using the Unified Soil Classification System (USCS).

Adjacent to the lobe, soil ranged from silty sand with gravel (SM) to sandy silt with gravel (ML), overlying chloritic schist bedrock averaging 3.7 m below the ground surface (bgs). In the undisturbed area to the south of FDL-A, the soil was ice-rich. Subsequent measurement indicated the average permafrost temperature adjacent to the lobe was -2.2° C and the permafrost table was approximately 0.6 m bgs. In contrast, the lobe consisted of frozen silty sand with gravel (SM) and silty gravel with sand (GM) and contained minor ice. The borehole that successfully penetrated the lobe indicated it was 26.4-m thick, overlying chloritic schist bedrock. Subsequent temperature measurements indicated the permafrost table was between 2 and 2.5 m bgs on FDL-A, and averaged -1.1° C below the depth of zero amplitude (Darrow et al., 2013). In one 30.5-m deep borehole (i.e., TH12-9004; see Figure 2.1), we installed an automated slope movement measurement device called a MEMS-based in-place inclinometer (M-IPI), along with

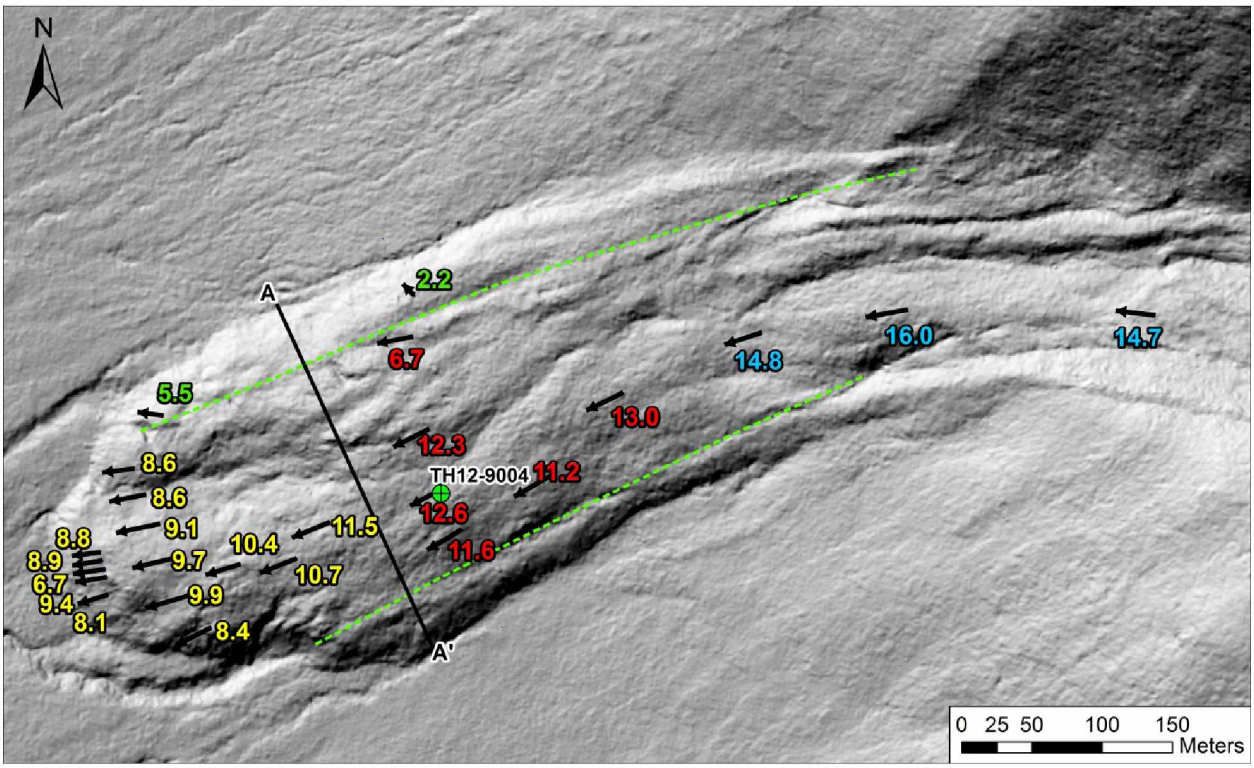

Figure 2.1. Surface movement of FDL-A, measured from October 2012 to March 2015. The arrows indicate the direction of movement for each marker and the numbers are the amount of movement in meters color-coded to correspond to average rates provided in Figure 3.1 (blue – upper lobe; red – middle lobe; yellow – lower lobe; green – levee). The green dashed lines indicate the location of the levees. A-A' is the location of the cross section for volume calculations. (Base map from Hubbard et al., 2011).

two vibrating wire (VW) piezometers and a thermistor string. Here, we focus on results obtained from this key boring.

Within the first month after installation, the M-IPI data indicated a shear zone located 20.6 to 22.8 m bgs at this location, as well as slow to moderate flow above the shear zone (Darrow et al., 2013). We placed the VW piezometers where we saw evidence of water pressure during drilling. Both piezometers recorded water pressure immediately after installation; the lower piezometer failed within 56 hours, likely due to the water pressure exceeding its range. The upper piezometer indicated a potentiometric surface about 10.8 m above the ground surface. By the end of October 2012, the casing and instrumentation within TH12-9004 sheared at 20 m. After shearing, we noted that the propylene glycol used to fill the casing had risen above the ground surface and was dripping out of the top of the casing. Additionally, the water pressure within the shear zone was high enough to cause fluid to enter into the insulation of the sheared thermistor string, travel up the boring and out to the data logger enclosure, where we observed fluid puddled at the bottom of the otherwise dry enclosure. These observations support the high pore water pressure measurements. Before shearing, the M-IPI measured approximately 79.2 cm of movement in 31 days (or approximately 2.5 cm per day), indicating a large increase in the rate of movement over the previous average rate determined from remote sensing analysis.

2.1.2 Surface Movement Measurements

In order to gather more information on the movement of FDL-A, we placed surface markers on the lobe in October 2012 for repeated measurements with a DGPS unit, having horizontal and vertical accuracies of ± 0.05 m. These markers formed a longitudinal transect and three cross-sectional transects, along with two control points on either side of the lobe.

Measurements were made twice in November 2012, and once in April 2013, June 2013, August 2013, June 2014, August 2014, and March 2015, respectively. During these trips to the study area, we also collected data from the instrumentation installed during drilling, and made visual observations of FDL-A.

2.2 GIS Analysis of FDL-A and Catchment

Landslide investigations are commonly performed using GIS analysis and high resolution imagery, and these investigations can assist in producing hazard assessments. Lyle and Hutchinson (2006) performed slope hazard identification and landslide inventory mapping in areas of degrading permafrost in the Yukon Territory, Canada. They looked at landslide attributes and primary controls on permafrost distribution, including slope angle, slope aspect, vegetation cover, and drainage conditions. While this study took place in an area that contained discontinuous permafrost, the same principles can be applied to areas of slope instability in continuous permafrost regions.

Following a similar approach as Lyle and Hutchinson, we completed a comprehensive GIS analysis of FDL-A, examining certain characteristics of the lobe and its catchment. The purpose of this analysis was to develop a procedure to serve as a guide for future analysis of other FDLs along the Dalton Highway corridor as additional high resolution imagery is obtained to identify similar elements that may contribute to the formation and movement of these features. We hypothesize that a statistical analysis of these attributes may yield correlations to the lobe's formation and movement. The components of this analysis included examining the surface area and slope angle of the catchment and the lobe, slope aspect and rock type within the catchment, and vegetation coverage of both the catchment and lobe, based on the following rationale. The

surface area of the catchment contributing material to the lobe may correlate to the lobe size. Steeper slopes in the catchment affect how much debris contributes to the FDL, and slope angles on the FDL could affect the rate and mechanism of movement. Slope aspect of the catchment can affect permafrost conditions and thus the stability of the material, while rock types may correlate to the formation and amount of debris contributing to FDLs. Lastly, vegetation affects the conditions of permafrost and soil stability and also can indicate areas of movement on the lobe.

In addition to the FDL attribute analysis, we mapped scarps, longitudinal cracks, and surface drainage on FDL-A, and determined volume per unit width to estimate the amount of material traveling towards the highway. All analysis was conducted with ArcMap using Light Detection and Ranging (LiDAR) imagery of the project area acquired in 2011. The majority of this study used LiDAR bare earth, or last return data, which displays the ground surface. The highest hit, or first return data, which is associated with the first returned laser pulse, displays the highest feature in the landscape, and was used for the vegetation analysis.

2.3 Isotope Analysis

In August 2014, we collected samples of the exposed ice in the lower RTS near the left flank (see Figure 1.4a), as well as water samples from the creek and a puddle adjacent to FDL-A during a major rain event. During a trip to the field in March 2015, we collected two samples of snow, one collected near the uppermost surface measurement marker and another collected at the toe. These samples were submitted for analysis to the Alaska Stable Isotope Facility at the University of Alaska Fairbanks' Water & Environmental Research Center. The purpose of the isotope analysis was to determine the relative age of the ice, and thus identify its probable origin. Stable isotope data were obtained using continuous-flow isotope ratio mass spectrometry

(CFIRMS). The δ^2H and $\delta^{18}O$ values were measured using pyrolysis-EA-IRMS. This method utilized a ThermoScientific high temperature elemental analyzer (TC/EA) and Conflo IV interface with a DeltaV^{Plus} Mass Spectrometer. Stable isotope ratios were reported in δ notation as parts per thousand (‰) deviation from the international standards, V-SMOW (Standard Mean Ocean Water). Typically, instrument precision is <3.0‰ for hydrogen and <0.5‰ for oxygen.

2.4 Laboratory Testing of Strength Parameters

We performed direct shear testing on frozen samples to determine the internal friction angle and cohesion of the FDL-A soil. We chose this testing method based on the amount of soil sampled and relative ease of conducting tests on frozen samples. The samples were obtained during the September 2012 drilling program using a split-spoon sampler, and were transported and stored in a freezer until testing could be carried out. All samples were taken from TH12-9004 in which all soil tested classified as silty sand with gravel (SM). The direct shear tests, following ASTM D3080-90 (1990), were carried out in a cold room to maintain the frozen state of the soil throughout testing. To ensure as little temperature fluctuation as possible, we modified the direct shear device by constructing an insulated box around the main shearing apparatus in which temperatures were monitored during testing. Additionally, we adjusted the rate of testing to simulate the lobe's rate of movement. Due to limitations in controlling near-freezing temperature settings, the cold room temperature was set to the warmest sub-freezing temperature it would maintain, which was -1.49° C and about 0.4° C colder than what we measured within the lobe. The insulated box helped to maintain this temperature within ± 0.05° C.

Using the average rate of movement of 2.5 cm per day from the October 2012 M-IPI data, three series of tests were performed on samples taken from 12.3 m, 13.9 m, and 24.7 m bgs.

Each sample was cut to a length of 2.54 cm to fit into the shearing box. The normal stresses applied were calculated using the overburden weight of the soils above the center of the shear zone. Then this normal stress (i.e., 441 kPa) was divided in half and doubled in order to perform three tests within one series. This resulted in normal stresses of 220.5, 441, and 882 kPa. The number of tests performed for each series was determined by the amount of soil samples available.

2.5 Slope Stability Analysis

We performed a slope stability analysis using SLOPE/W 2007 software, which utilizes a limit equilibrium approach (GEO-SLOPE International LTD., 2008). To produce the geometry of FDL-A for the slope stability analysis, the LiDAR digital elevation model (DEM) was used to create a profile of the lobe surface. The bedrock surface underneath the lobe was estimated using the known bedrock depths from the boreholes on the lobe and in the undisturbed area to the south, as well as natural bedrock exposures in the catchment area and the general nature of the slope surface created by a second profile off the lobe. The pore water pressure was estimated using the measured value within the lobe, and the bedrock was defined as impermeable without having any pore water pressure. Historic earthquake information and a map of ground motion hazard values produced by the U.S. Geological Survey were used to determine the seismic load for this analysis (Alaska Earthquake Center, 2013; Wesson et al., 2007). In the last 115 years, 90 earthquakes occurred within a 100-km radius of FDL-A. These earthquakes had an average magnitude (M) of M3.5, with a M5.5 as the largest event. Based on this information, we used a horizontal acceleration of 0.15g for this analysis.

CHAPTER 3 RESULTS

3.1 Subsurface and Surface Movement Analysis

From October 2012 to March 2015, the average total movement on FDL-A was approximately 10.5 m, with an average rate of 4.4 meters per year. The upper portion of FDL-A demonstrated the most movement, between 14.7 and 16.0 m, while the rest of the lobe moved between 6.7 and 13.0 m during this time frame (see Figure 2.1). We also observed from these surface measurements that FDL-A has formed levees that move at a slower rate and constrain its lateral flow (Darrow et al., 2015); the levee surface marker movements are not included in the overall average rate. FDL-A's rate of movement not only varies spatially, but it also changes throughout the year (see Figure 3.1). Our surface measurements indicate that rates are highest during the fall season, decreasing with the onset of winter. Rates then begin to increase in the spring and continue increasing throughout the summer months. Lack of snow during the early winter of 2012 caused an overall cooling of the lobe, which may have resulted in the low rates measured in June 2013. Since that time, the surface movement rate has increased, with the upper lobe moving about 1 cm per day faster than the lower lobe. Unfortunately, as the surface measurements are dependent on the limited number of trips made to the field, they lack temporal resolution; however, the trends in the data indicate that a relationship between temperature and movement exists, with FDL-A moving faster when it reaches both maximum thawing and internal temperature and moving slower when minimum temperatures are reached.

Despite the shearing of the M-IPI in 2012, the upper portion of the device continues to record slope movement and temperature data; however, we no longer have a fixed reading below the shear zone. Surface measurement data collected using the DGPS were used to determine the

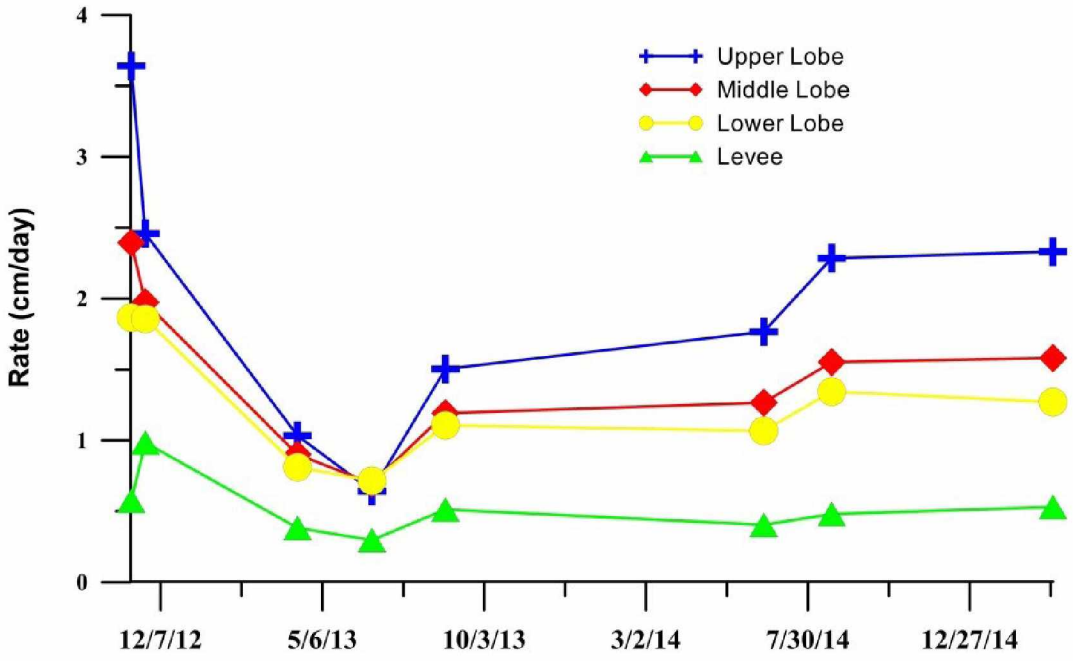

Figure 3.1. Rate of movement trends for FDL-A.

surface location of the uppermost measurement and to establish the location of the M-IPI device in space (Darrow et al., 2015). Figure 3.2a is a summary of this corrected data from October 27, 2012 until August 21, 2014. Since September 2012, when the instrument was installed, the top of the casing and the M-IPI device moved 9.8 m downslope (Darrow et al., 2015).

The data presented in Figure 3.2b is from the portion of the M-IPI that is still functioning. This does not include any movement within or below the shear zone. The data indicate an ongoing leaning of the instrument downhill, with a greater amount of leaning near the surface. In addition to the leaning, two anomalous zones are present in the casing at 7.6 m and 16.3 m bgs. A diagram of the boring log in Figure 3.2c is presented for comparison. The disturbance at 7.6 m bgs (indicated by upper arrow) corresponds to where we lost fluid during drilling and grout during backfilling the boring. The lower disturbance (indicated by the lower arrow) corresponds to where evidence of water pressure was observed during drilling. These anomalous areas may represent additional shear zones, or sagging or buckling of the casing within voids located at these depths (Darrow et al., 2015).

Monthly rates of movement and corresponding temperatures collected from the M-IPI are presented in Figure 3.3. As with the surface marker measurements, these data also indicate that the internal movement below the active layer (i.e., greater than 2.5 m bgs) steadily increases with time until September (see Figures 3.3a and 3.3d), at which point the internal flow rate steadily decreases until March (see Figure 3.3b). Then the cycle repeats the following spring (see Figures 3.3c and 3.3e). The rate of movement within the active layer becomes significantly higher during the summer as the active layer thaws. During late summer and early fall, the highest rate of movement occurs in a zone between the surface and the permafrost table (Darrow et al., 2015).

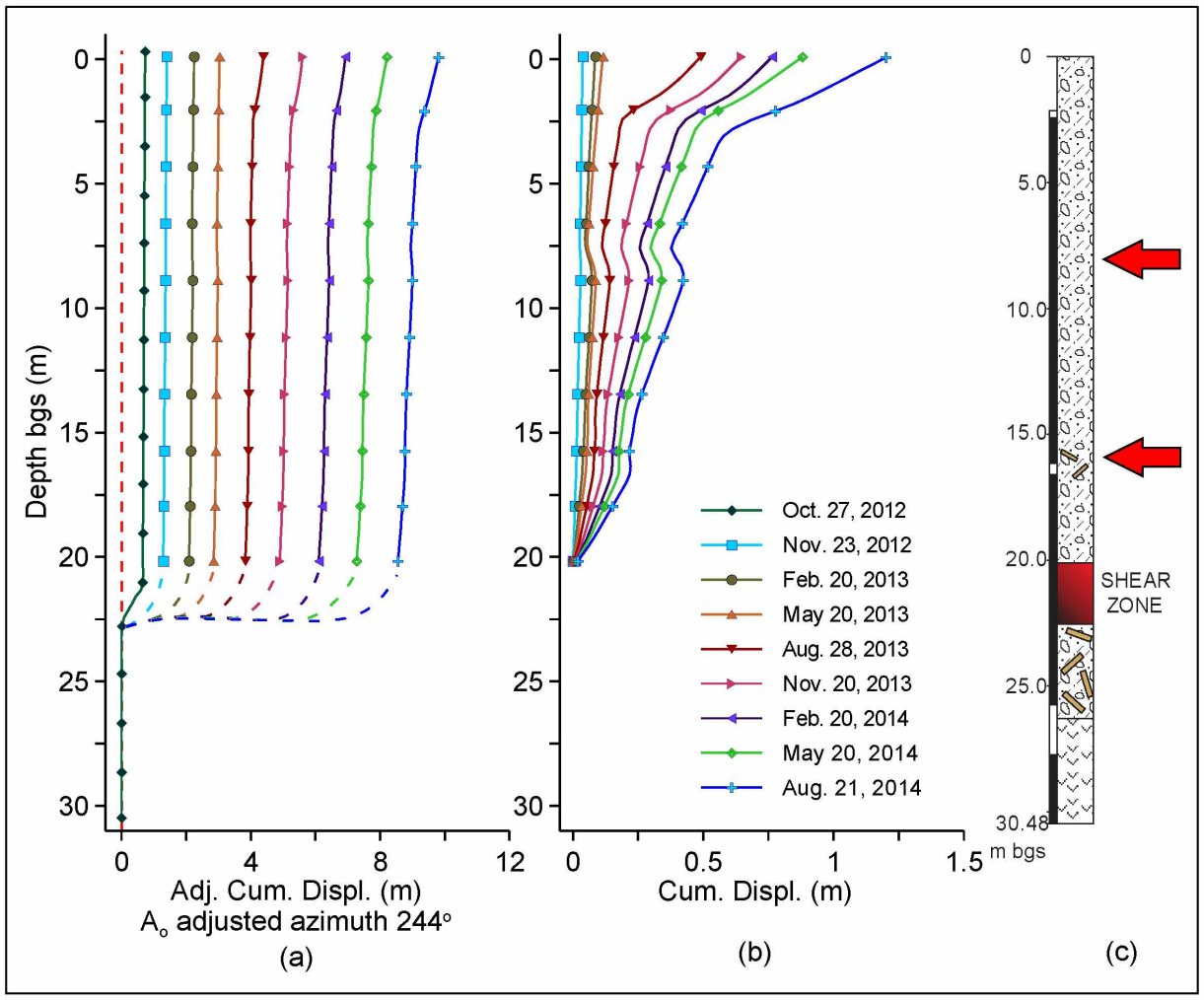

Figure 3.2. Cumulative displacement measurements. The shear zone is approximately located in (a) with dashed lines. The data in (a) were adjusted to include all post-shearing movement based on the surface measurements. The data in (b) show only movement measured above the shear zone at 20.6 m bgs. The boring log in (c) indicates the shear zone with a red rectangle. Wood fragments are shown as brown rectangles and the bedrock surface is at 26.4 m bgs. Frozen ground is represented by the black bar along the left side of the log with the white portions representing questionably frozen areas (Darrow et al., 2015).

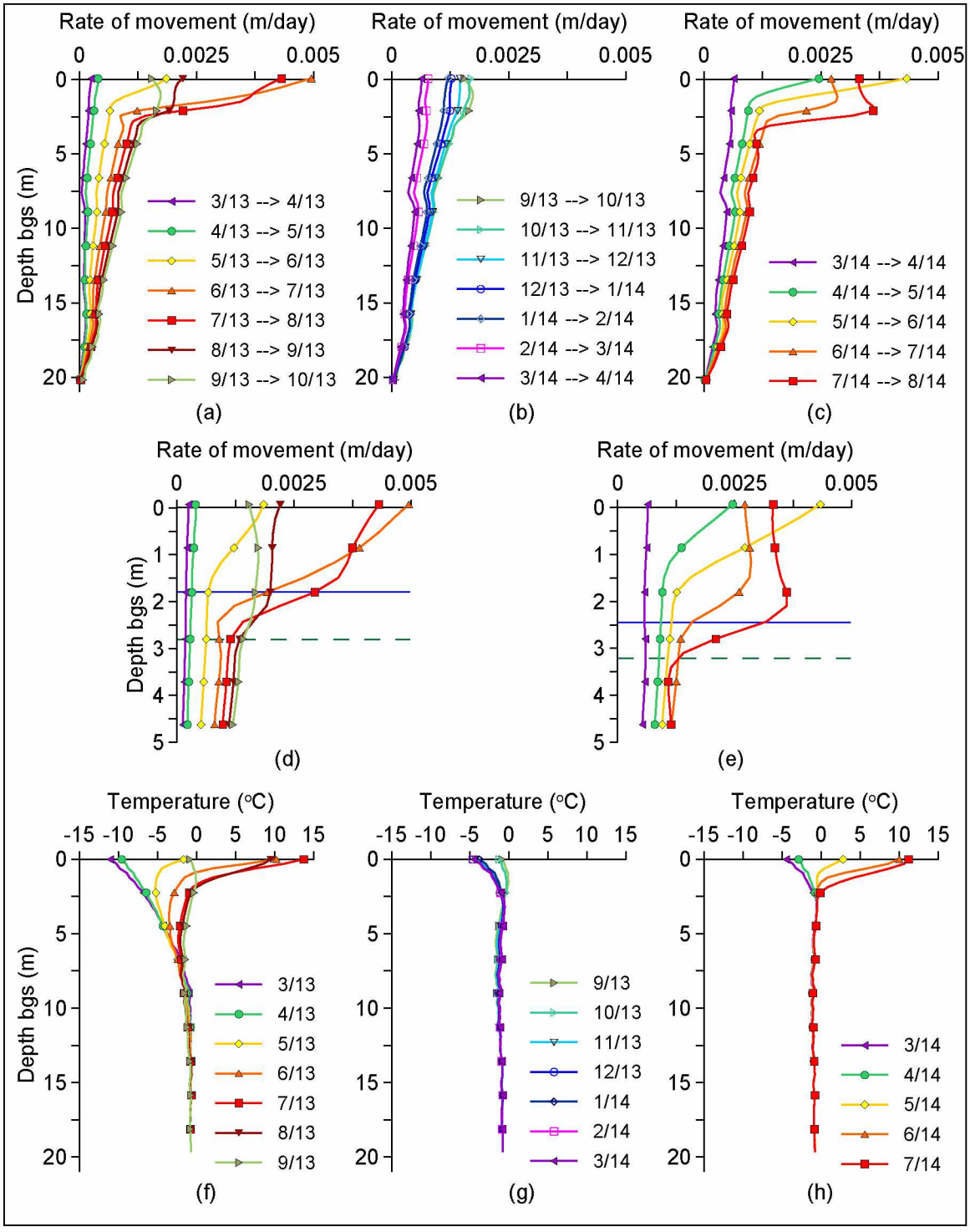

Figure 3.3. Daily rate of movement (a-e) and subsurface temperatures (f-h) of FDL-A, as measured by the M-IPI device. Data show the average daily rate by month and periods are broken into spring through fall of 2013 [(a), (d), (f)], winter of 2013/2014 [(b) and (g)], and spring through summer of 2014 [(c), (e), (h)]. Graphs (d) and (e) are close-up views of the upper 5 m; the blue horizontal line indicates the active layer depth and the green dashed horizontal line is the depth at which movement rate increases. (Darrow et al., 2015).

In other words, the highest rate of movement becomes sandwiched between the cooling surface and the colder permafrost below.

The M-IPI device also contains temperature sensors that we have relied on for data since the failure of the thermistor string during shearing. Data collected from these sensors are presented in Figures 3.3f through 3.3h. As mentioned earlier, snowfall was below normal during the early winter of 2012/2013, which contributed to colder ground temperatures as compared to the warmer temperatures during the winter of 2013/2014. Additionally, these data indicate that the rate of movement within FDL-A is highly dependent on temperature, as a direct correspondence exists between higher rates of movement and higher temperatures (Darrow et al., 2015).

3.2 GIS Analysis of FDL-A and Catchment

We first delineated the boundaries of FDL-A and its catchment using the LiDAR imagery and observations made in the field (Hubbard et al., 2013). We developed a triangulated irregular network (TIN) using the LiDAR bare earth DEM. This was utilized to find the surface area of the catchment and FDL-A, which were 926,017 m^2 and 306,687 m^2, respectively. For the catchment of FDL-A, we investigated the aspect, slope, and geology. Aspect and slope rasters were developed from the bare earth DEM (see Figure 3.4), while feature classes based on field observations were used to delineate geology (see Figure 3.5).

Tables 3.1 and 3.2 contain summaries of the calculated percentages of the slope angle and aspect, and coverage of geological units within the catchment, respectively. The majority of the catchment has slope angles between 20° and 40° with most of the catchment having a southwest to northwest aspect. Based on the geologic map analysis, the most common rock types found in

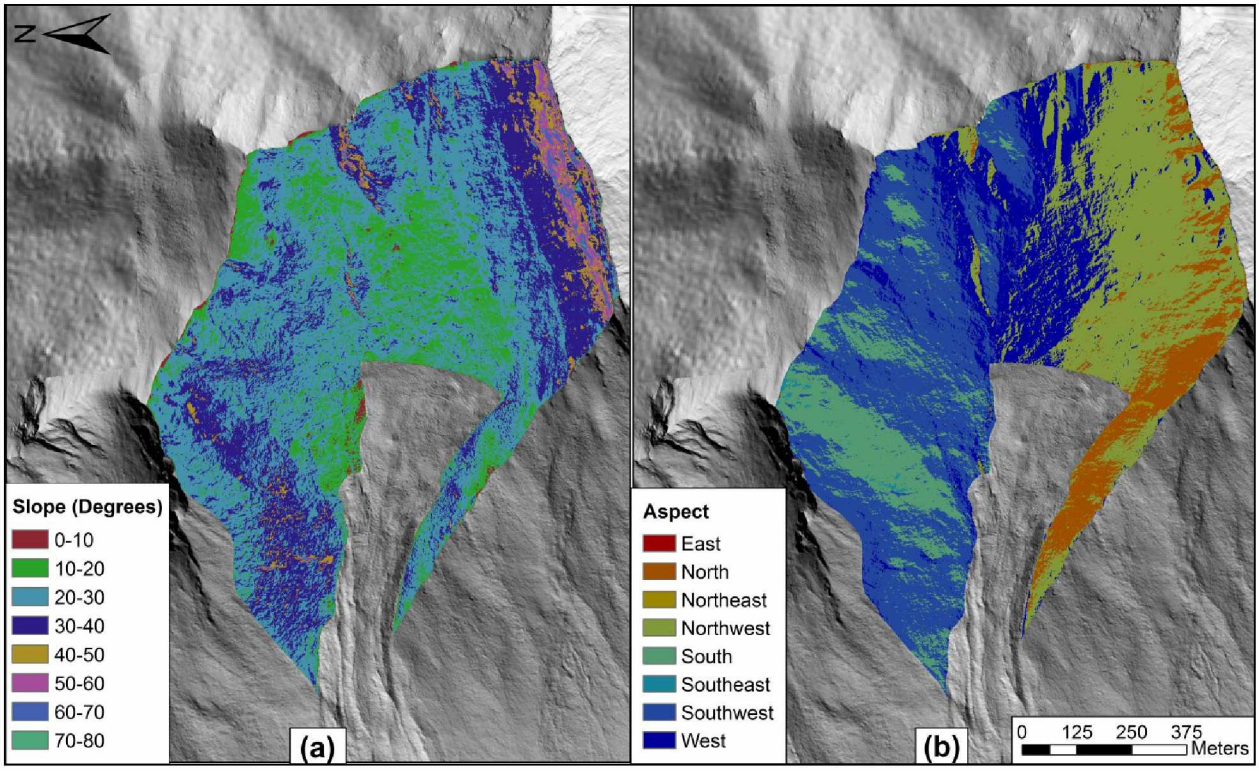

Figure 3.4. Slope (a) and aspect (b) analysis results of FDL-A's catchment. (Base map from Hubbard et al., 2011 and GINA, 2001).

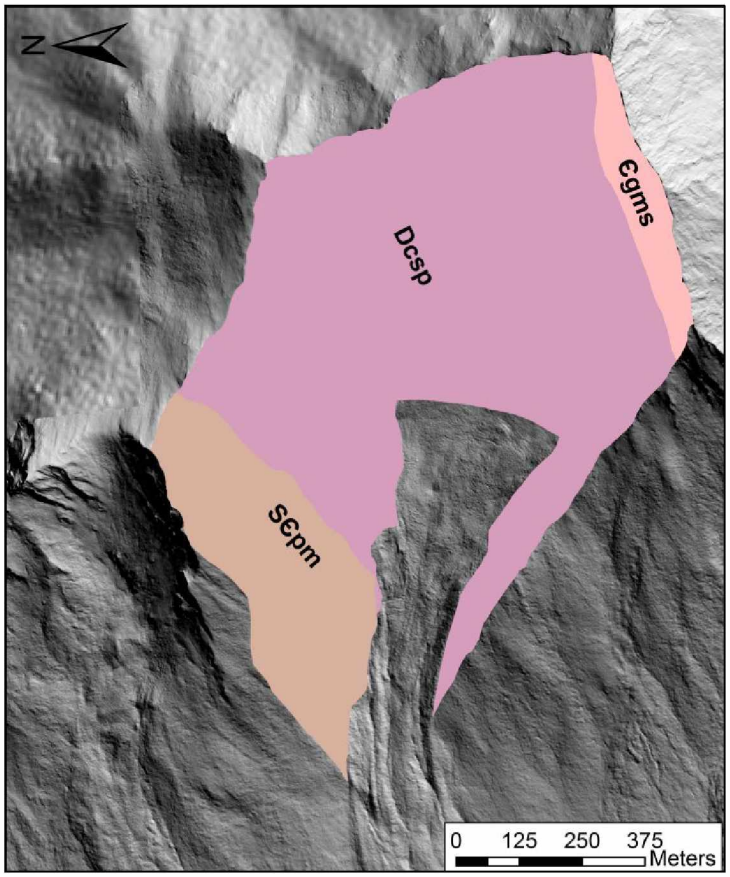

Figure 3.5. FDL-A's catchment geology. See Table 3.2 for unit descriptions (Base map from Hubbard et al., 2011 and GINA, 2001; geological unit data from Spangler and Hubbard, 2015).

Table 3.1. Percentages of FDL-A's slope angle (for lobe and catchment) and aspect (for catchment only).

Lobe		Catchment			
Slope (°)	Percentage	Slope (°)	Percentage	Aspect	Percentage
0-10	13.4	0-10	0.8	North	8.2
10-20	53.2	10-20	16.1	Northeast	0.2
20-30	27.6	20-30	50.1	East	0.1
30-40	5.4	30-40	26.7	Southeast	0.3
40-50	0.4	40-50	3.7	South	13.1
---	---	50-60	1.9	Southwest	32.3
---	---	60-70	0.7	West	17.6
---	---	70-80	0.0	Northwest	28.2

Table 3.2. Geological unit percentages for FDL-A's catchment. Descriptions from Dillon et al. 1988, Mull and Adams, 1989, and Spangler and Hubbard, in review.

Geological Unit	Description	Percentage
Є€gms	Interbedded, platy to massive, gray-brown to green greywacke, metasandstone and metasiltstone	5.2
Dcsp	Predominately interbedded, platy, purple and green-blue chloritic schist and phyllite; subordinate black to gray phyllite	75.9
S€pm	Predominately interbedded, platy, brown to gray-black phyllite, metasiltstone, metasandstone and greywacke; subordinate shale	18.9

the catchment are chloritic schist and phyllite, which correspond with the type of rock debris that we have observed on the lobe itself. The unit Ꞓgms has the highest slope angles (see Figure 3.4b), but makes up a very small percentage of the catchment. The majority of the area underlain by the two remaining geological units has slope angles between 10° and 40°.

Vegetation coverage in the catchment was determined by subtracting the bare earth from the highest hit elevations, resulting in the vegetation height. In the field, we observed that any significant vegetation on FDL-A and in its catchment was taller than 1 m; thus, brush shorter than 1 m was eliminated in this analysis (see Figure 3.6). The vegetation observed in the catchment greater than 1 m is mainly spruce, with some alder and willow. The upper lobe is vegetated mainly by alder and willow between 2- and 4-m high with scattered spruce. Towards the toe, the spruce trees become more abundant and reach heights up to 20 m. The percentage of vegetation coverage in the FDL-A catchment was found using the Block Statistics tool in ArcGIS. Most of FDL-A's catchment has little or no vegetation as seen in Figure 3.6a. The areas with the most vegetation are on west-, south-, and southwest-facing slopes that are between 10° and 30°. The steeper-sloping areas and those facing east and north support little vegetation, if any. This analysis indicates that the very steep area on the south part of the catchment supports vegetation; however, this is most likely an anomaly in the LiDAR data due to the very high slope angles, as field observations indicate that this area is sparsely vegetated. A vegetation analysis was done for the lobe itself using the same methods (see Figure 3.7). Many of the areas with low vegetation coverage on the lobe can be associated with zones of movement and instability that we have observed. Examples include the two RTS areas (see the yellow arrows in Figure 3.7b), and the large scarp near the toe on the left flank of the lobe (see the black arrow in Figure 3.7b).

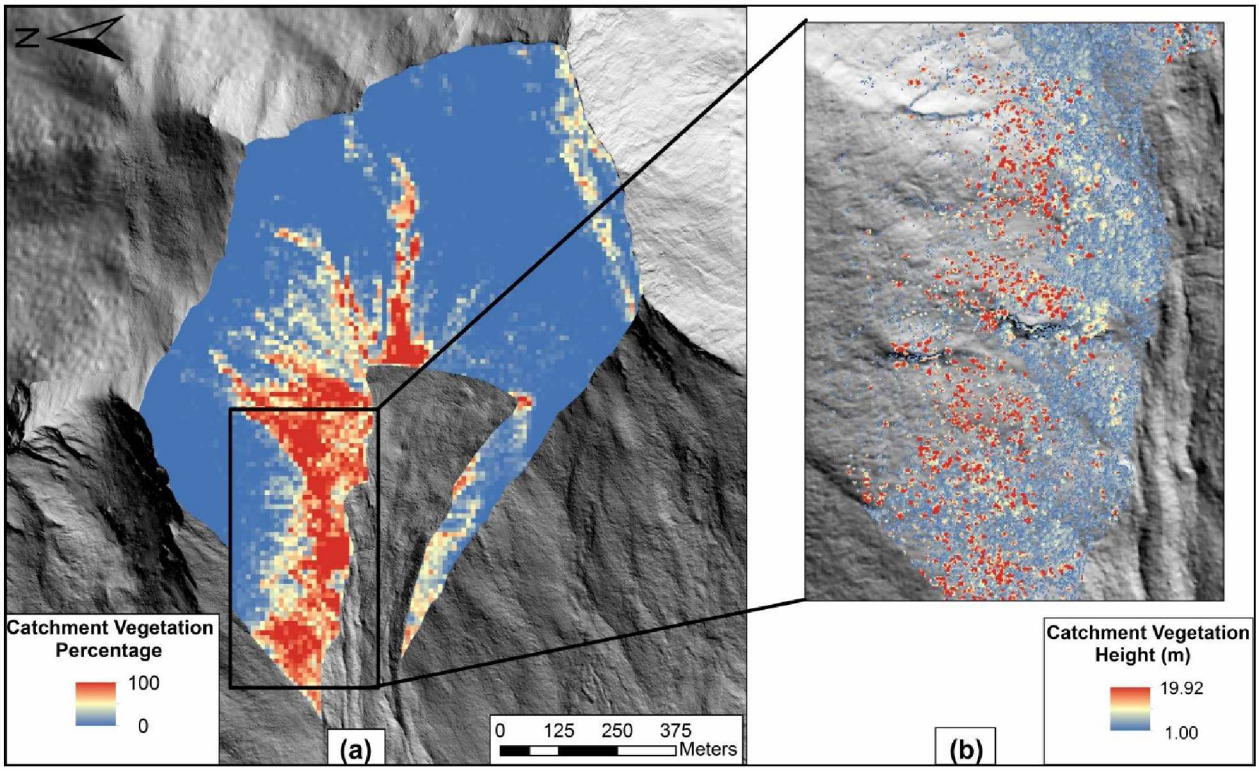

Figure 3.6. FDL-A catchment vegetation analysis results: (a) is percentage of vegetation coverage, and inset (b) is vegetation height in a highly vegetated area. (Base map from Hubbard et al., 2011 and GINA, 2001).

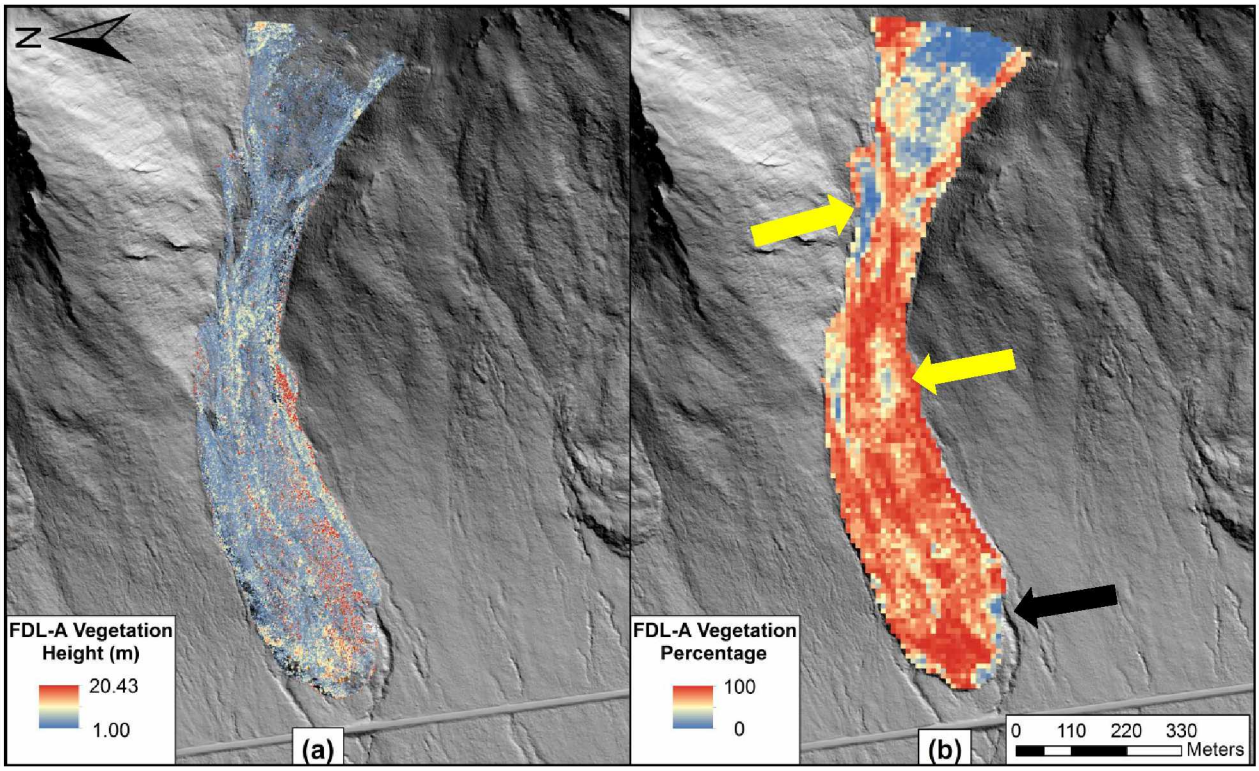

Figure 3.7. FDL-A lobe vegetation analysis results: (a) is vegetation height, and (b) is percentage of vegetation coverage. The yellow arrows indicate the retrogressive thaw slump locations, and the black arrow indicates the large scarp and actively eroding area on the left flank. (Base map from Hubbard et al., 2011).

A slope analysis was performed on the surface of FDL-A, and the results are presented in Figure 3.8 and Table 3.1. The majority of the lobe surface has a slope between 10° and 20°, with the steepest slopes (i.e., between 30° and 60°) occurring along the right and left flanks, around the toe, and within some of the longitudinal cracks. A careful visual study of Figure 3.8 suggests that steeper areas on the lobe surface form risers of lobate-shaped "steps". In the field, we also observed these smaller lobes on the larger FDL-A surface. These smaller surface lobes may be the result of the differential rate of near-surface movement observed in the M-IPI device data.

We also mapped several discrete surface features, including scarps, longitudinal cracks, and creeks on the lobe surface. Several techniques, such as surface roughness calculations, and analysis of multiple aspect and hillshade images at varying azimuths, were used in an attempt to define the cracks located along the length of the lobe. None of these techniques were successful, however, due to the highly variable surface of the lobe. Instead, we developed cross sections of the lobe on a 10-m spacing, from which we identified the locations of substantial cracks (i.e., greater than 2-m wide). These crack locations then were plotted and connected on the LiDAR image. Figure 1.4a displays the center lines of the cracks, while outlines of the cracks are presented in Figure 1.4b to illustrate the amount of separation. A similar approach was used to map scarps by creating profiles along the length of the lobe. We verified the locations of several of these cracks and scarps in the field during the summer of 2013, and also mapped additional scarps.

As mentioned previously, the creek draining the surface of FDL-A changed its channel location in recent years. A flow accumulation was performed using the LiDAR DEM to map the original channel location, which drained to the west. In 2013, we took handheld GPS coordinates along the new channel draining off the left flank of FDL-A to the southwest (see Figure 1.4a).

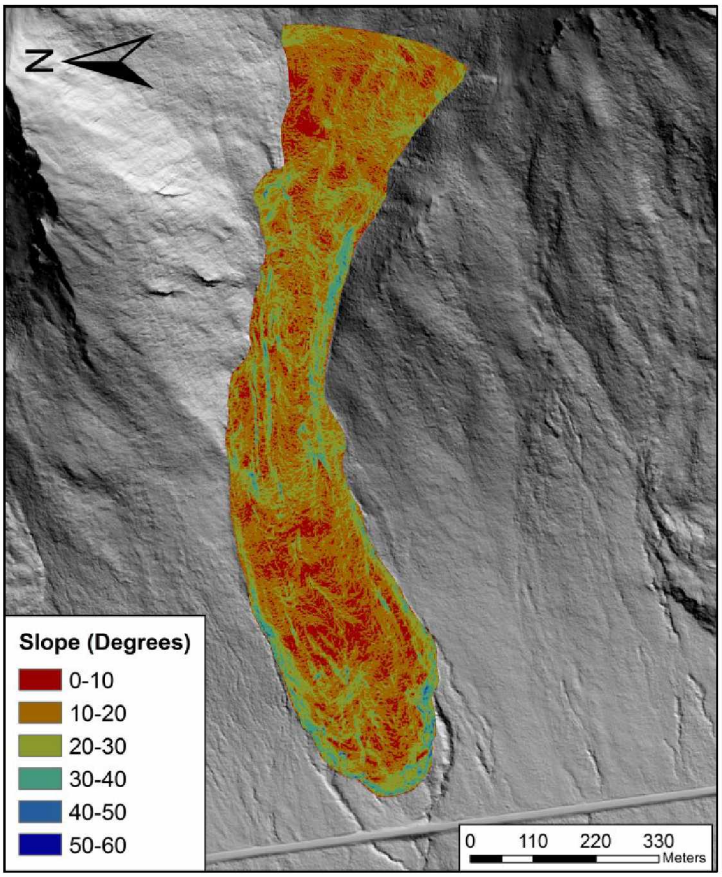

Figure 3.8. Results of FDL-A lobe slope analysis. (Base map from Hubbard et al., 2011).

To estimate the amount of material that could contact the highway, we performed volume per unit length calculations by creating a cross section along the widest part of the lobe (see A-A' in Figure 2.1), thus yielding the most conservative volume estimate. The estimated volume in this 1-m deep cross section is 4,454 m^3 of material. Using the average measured moist unit weight of 21.2 kN/m^3, this is equivalent to 94,417 kN or approximately 10,613 US short tons. With the average rate of movement at 1.2 cm per day, an estimated 46,872 tons of material per year will come into contact with the highway based on this cross section location.

3.3 Isotope Analysis and Ice Formation

Although we did not intercept any massive ice during the 2012 subsurface investigation, we have observed the presence of massive ice within unstable areas along the margins of several FDLs. While there are several different origins of massive ice in periglacial regions (Davis, 2001; Washburn, 1985; Williams and Smith, 1989), we hypothesize that this massive ice is infiltration ice, which forms as snow melt and rain quickly freeze after entering into cracks in the ground (Kanevskiy and Shur, pers. comm., 2014). The term "infiltration ice" has been used to describe a similar phenomenon produced as summer melt infiltrates glacial ice (Tarussov, 1992). The ice we observed in the head scarps of the RTS was clear consisting of large crystals, and contained some bubbles and strands of fungus (see Figure 3.9). Observations of the head scarp in the lower RTS further support the infiltration ice origin. In Figure 3.9a, the exposed massive ice is indicated in the center of the photograph. To either side of the massive ice, we noted a buried organic layer that was vertically offset. Further investigation of the surface indicated that the location of the massive ice corresponded with a surface crack.

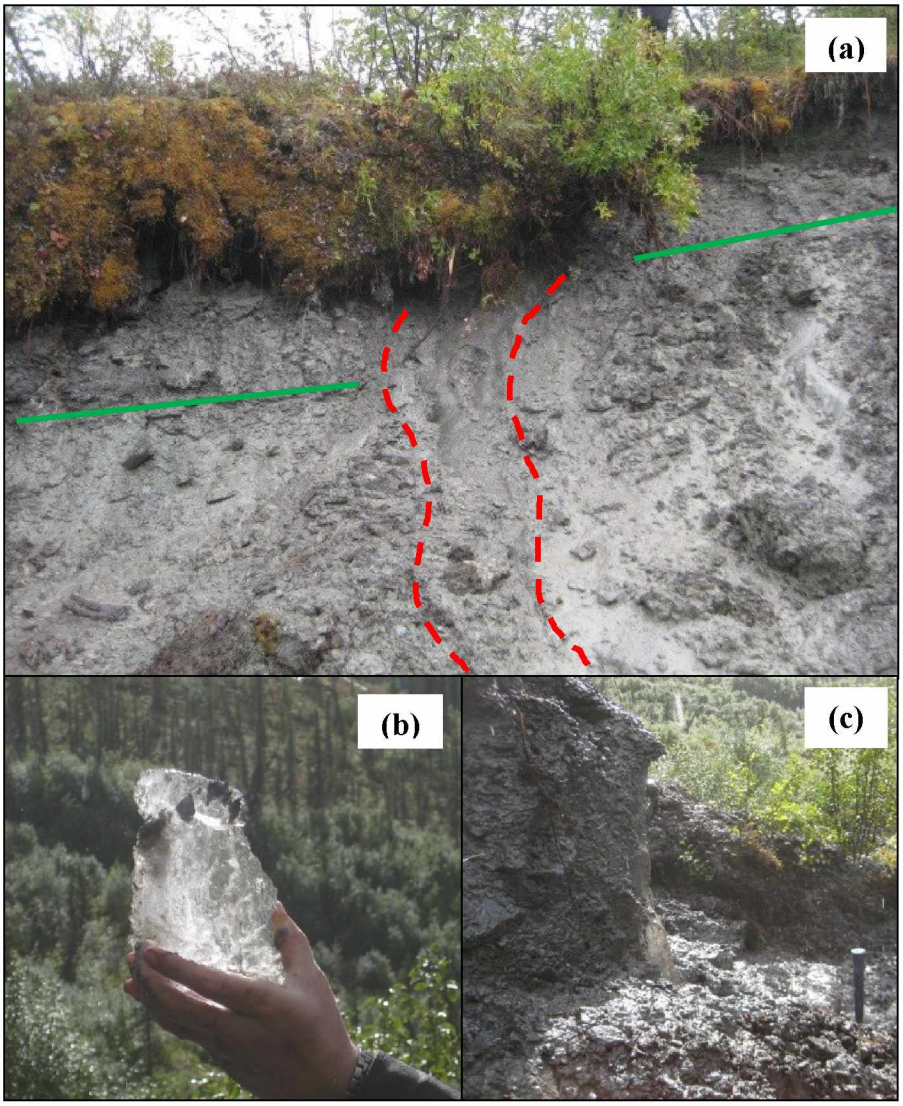

Figure 3.9. Field observations from August 2014. (a) Head scarp in retrogressive thaw slump along the left flank with exposed massive ice in a transverse crack (outlined by red dashed lines) and offset buried organic layers (indicated by solid green lines); (b) clear infiltration ice from head scarp of retrogressive thaw slump; (c) retrogressive thaw slump with exposed massive ice in lower catchment area.

Figure 3.10 is a presentation of the isotope analysis results, with the Global Meteoric Water Line (GMWL) plotted for comparison. The infiltration ice sample plots close to the average of the creek and puddle samples collected during the 2014 summer. The average of the snow samples is somewhat lighter. Isotope values from massive ice bodies taken from the literature also are presented in Figure 3.10. These include values from Pleistocene wedge ice near Fairbanks, Alaska (Douglas et al., 2011), lateglacial and Holocene wedge ice near Barrow, Alaska (Meyer et al., 2010), and a suite of wedge ice samples ranging in age from Pleistocene to recent from northern Siberia (Meyer et al., 2002). This collection of data indicates that the oldest ice has the lightest isotopic composition, which becomes heavier with decreasing age. Most notable is that the infiltration ice sample from FDL-A is bracketed by recent and subrecent wedge ice. The heavy isotopic composition of the infiltration ice and its similarity to the creek and puddle samples further supports the hypothesis that infiltration ice forms from rain water (and to a lesser extent snow melt) entering into cracks open at the surface. It should be noted that infiltration ice differs in formation from wedge ice. Wedge ice forms from water entering into a small crack in the ground during winter. Its expansion upon freezing widens the crack, with the crack growing in size over time as the process repeats itself. In the case of infiltration ice, a large crack may form at any time of the year due to movement within the FDL. Water enters the crack, and while it still expands upon freezing, this lateral expansion is minor compared to the widening of the crack due to ongoing movement.

3.4 Laboratory Testing of Strength Parameters Results and Analysis

Each direct shear test took approximately 12 hours to complete using the slow shearing rate of 2.54 cm per day. The samples were examined (see Figure 3.11) at the end of each test and

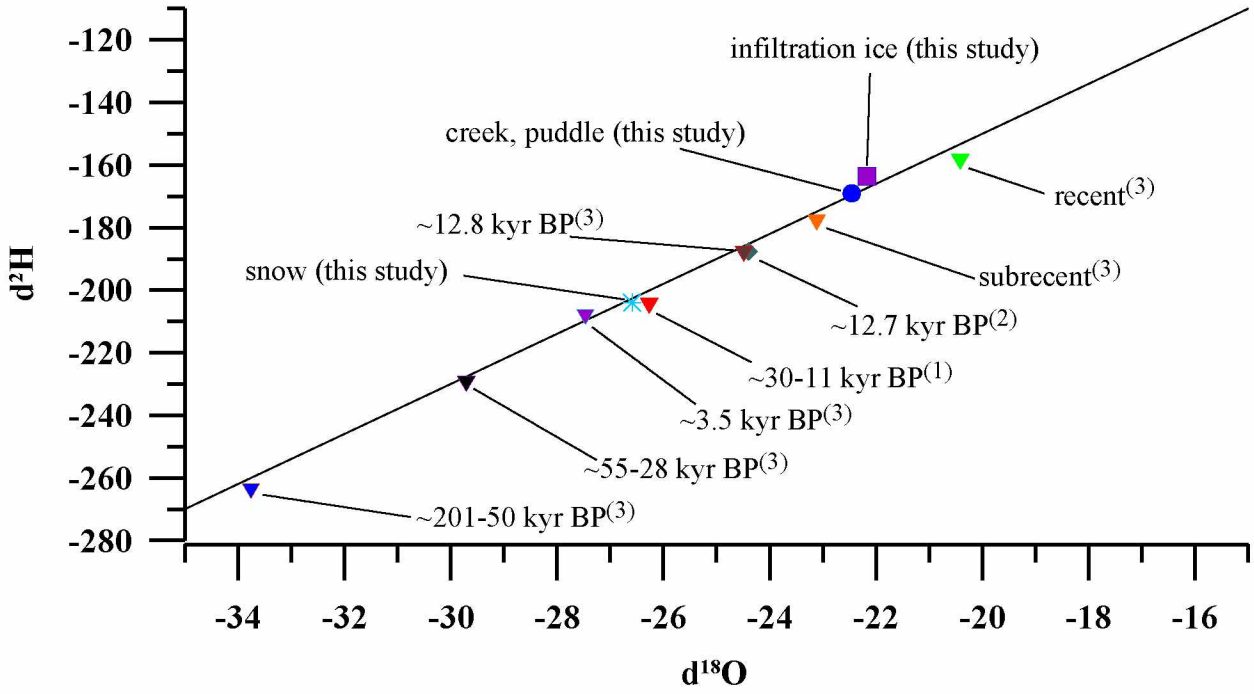

Figure 3.10. Isotope analysis results. The GMWL is plotted for comparison. Diamond and upside-down triangle symbols represent wedge ice sample values; values taken from the literature are from Douglas et al., 2011 [(1)], Meyer et al., 2010 [(2)], and Meyer et al., 2002 [(3)].

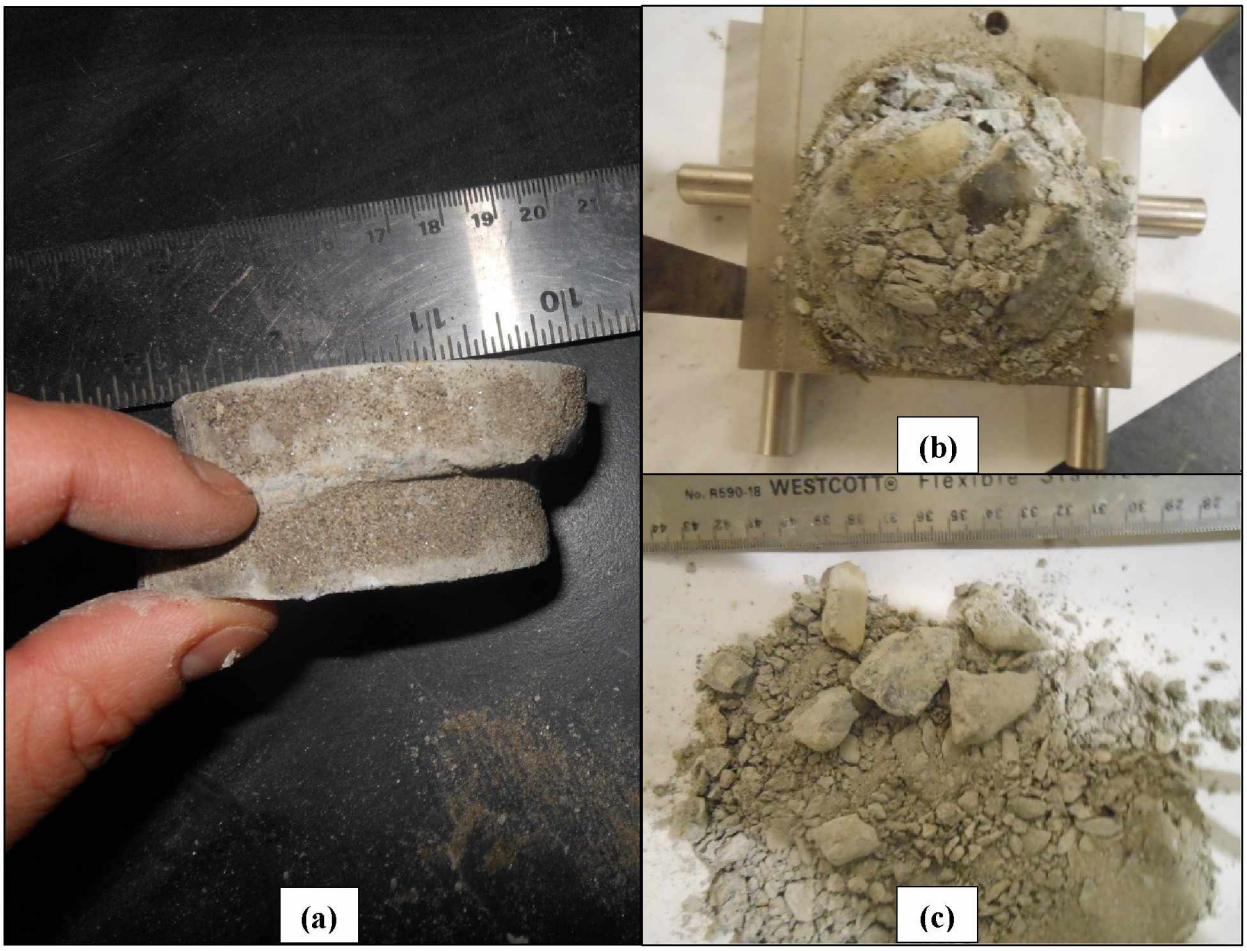

Figure 3.11. Frozen soil samples after direct shear testing: (a) successfully sheared sample; (b) large rock fragments pulverized the upper portion of the sample in a failed test; (c) most fragments of rock in the failed samples measured at least 3 cm in length.

oven-dried to obtain their moisture content according to ASTM D2216-90 (1990). One of the three series of tests failed; upon examination of the samples, we observed that each sample contained large rock fragments (see Figures 3.11b and 3.11c). This resulted in the pulverization of the upper portion of the sample as the test progressed. Results from the direct shear testing are presented in Figure 3.12 and Table 3.3. While all the soil tested from this borehole classified as silty sand with gravel (SM), visual observations of these samples indicated some differences. Sample 12-2515, from a depth of 12.3 m bgs, was fine-grained with some small rock fragments and no significant amount of ice was visible. Sample 12-2521, which was from 24.7 m bgs and close to the shear zone, did not contain as many rock fragments and had a noticeable amount of ice, which is indicated by higher moisture contents. The differences in the peak and residual internal friction angles of the two samples were not significant; however, sample 12-2521 demonstrated higher peak strength results and a larger difference in the peak and residual cohesion.

3.5 Slope Stability Analysis Results

For this analysis, the unit weight, cohesion, and internal friction angle for the bedrock were estimated using published values (Gonzalez de Vallejo and Ferrer, 2011). The properties of the frozen silty sand with gravel found within the lobe were determined directly from laboratory testing and averages of short-term frozen direct shear testing results (see Table 3.4); however, these values did not take into account the time-dependency of frozen soil. The strength of frozen soil varies with loading rate, as faster loading rates result in increased strength. Due to this time-dependent component, long-term strength is generally much smaller than short-term strength. The period of time in which laboratory testing is usually performed is seldom long enough to measure what would be representative of long-term strength (Scher, 1996). Depending on the

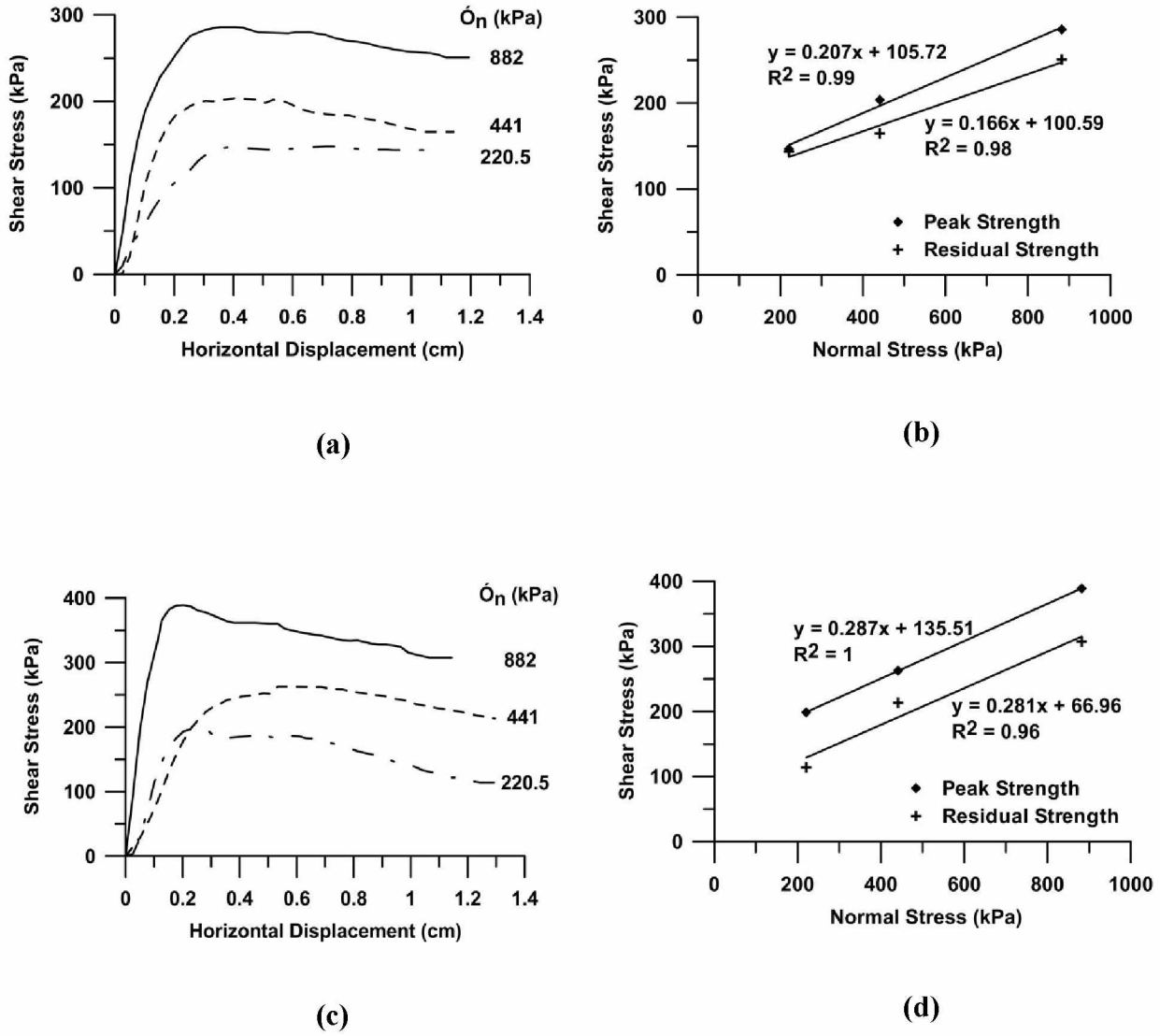

Figure 3.12. Results from direct shear testing of two frozen samples taken from FDL-A: (a) and (c) are shear stress and horizontal displacement for Samples 12-2515 and 12-2521, respectively, (b) and (d) are shear stress and normal stress for Samples 12-2515 and 12-2521, respectively. Resulting friction angles and cohesion values, and corresponding volumetric moisture contents, are listed in Table 3.3.

Table 3.3. Direct shear results for FDL-A frozen soil samples. Volumetric moisture content values show the range for three samples in each test series.

Sample	Volumetric Moisture Content (%)	Cohesion (kPa)	Internal Friction Angle (°)
12-2515	18.2 - 22.6	106 (Peak) 101 (Residual)	11 (Peak) 10 (Residual)
12-2521	31.8 - 49.6	136 (Peak) 67 (Residual)	16 (Peak) 16 (Residual)

Table 3.4. Material properties used in the slope stability modeling. The * indicates material properties taken from Gonzalez de Vallejo and Ferrer (2011).

Material	Unit Weight (kN/m^3)	Cohesion (kPa)	Internal Friction Angle (°)
Silty sand with Gravel (SM)	21.2	120	13
Chloritic Schist*	26.5	8,500	25

type of soil, cohesion is significantly decreased from 1/15 to 1/2 of the short-term strength, while in frozen sand the friction angle is typically independent of the time of load action (Tsytovich, 1975; Vyalov, 1986). The short-term friction angle and cohesion for the lobe soil (see Table 3.4) initially used in this analysis resulted in a factor of safety greater than 1.00.

In landslide studies, the long-term soil strength properties are often determined through a back analysis due to difficulties encountered with laboratory tests. In such an analysis, adjustments are made to the strength properties and when the factor of safety is equal to 1.00, the conditions represent a reasonable model of the failure (Duncan, 1996). To conduct this type of evaluation on FDL-A, several sensitivity analyses were performed. We varied the friction angle over the range of values determined from the direct shear testing (10° to 16°) and assumed that it did not vary more than this due to the sandy nature of the soil. Using this range of friction angles, we determined that the cohesion values resulting in a factor of safety of 1.00 ranged from 43 to 53 kPa, which are between 1/2 and 1/3 of the short-term strength and lie within the ranges reported by Tsytovich (1975) and Vyalov (1986) for long-term strength. Even with the higher friction angle values, any decrease in cohesion significantly decreased the factor of safety.

The SLOPE/W software includes several methods to establish the location of the shear zone. For this analysis, a fully specified shear zone was projected in the model and then optimized by the program. The optimized shear zone demonstrated a failure surface ranging from 0.1 to 1.0 m above the bedrock surface in the upper part of the lobe. In the region of the lobe where the shear zone is known, the optimized results indicated a failure surface traveling through this known point. Figure 3.13 is an overview of the geometry used for the analysis, along with the optimized shear zone location at the toe, at the location of our boring, and in the upper portion of the lobe. Along the profile from the head to the toe, the optimized shear zone was

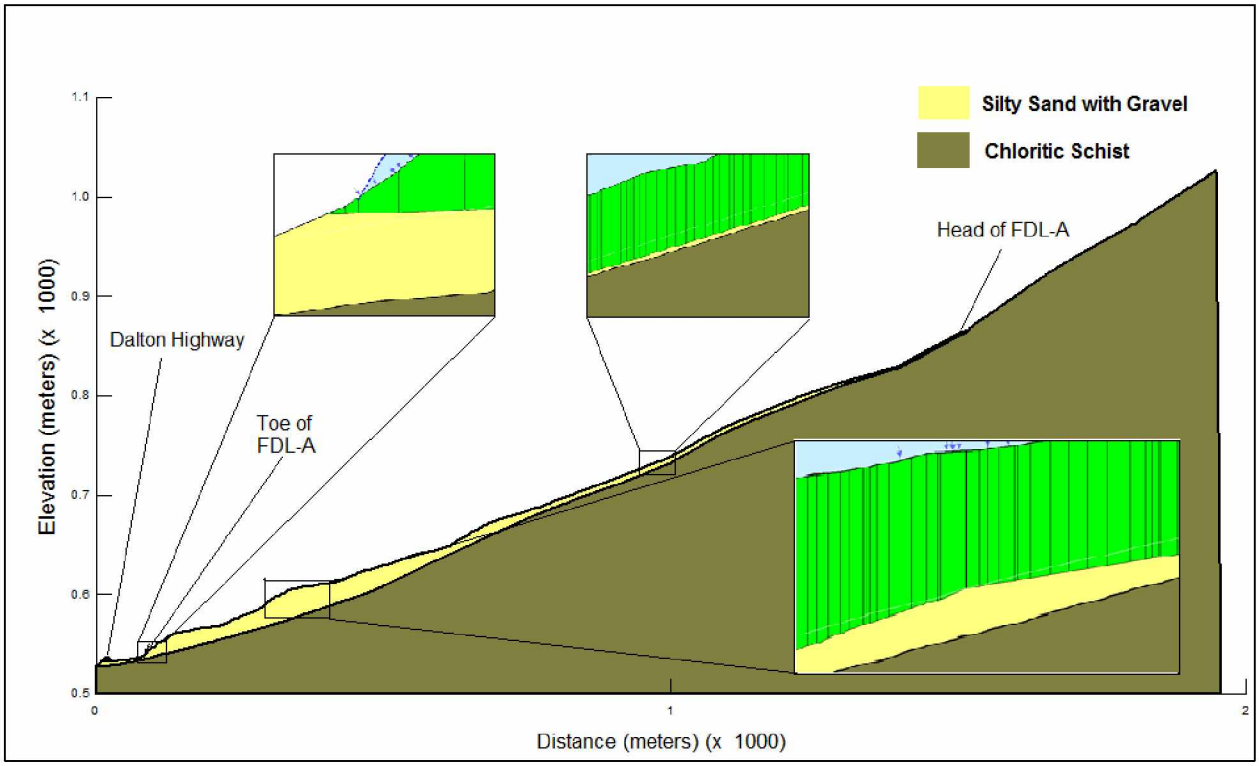

Figure 3.13. Profile of FDL-A used in slope stability analysis. The lower inset shows where the optimized failure surface travels through the known shear zone location. The upper left inset shows the failure surface exiting at the ground surface from the toe. The upper right inset shows the failure surface in a thinner area of the lobe. The green area indicates how the lobe material is divided into slices for the limit equilibrium analysis, and the bottom of these slices indicates the location of the critical slip surface.

located deeper in the lobe where the lobe itself was thin, and was located farther away from the bedrock surface where the lobe was thick. The shear zone exited at the toe more than 3 m above the bedrock (see inset in Figure 3.13).

To analyze the effects of pore water pressure on the factor of safety, we performed a sensitivity analysis on the pore water pressure ratio, R_u. This value is the ratio of the pore water pressure to the unit weight of the soil multiplied by the height of the soil column. This method of defining pore water pressure is not recommended for slope stability analysis unless it is for a very simple, isolated case (GEO-SLOPE International LTD, 2008). While the complicated nature of the lobe and unknown pore water pressure throughout made the use of the R_u difficult for rigorous analysis, we assumed an average R_u value for the whole lobe to investigate how changes in the pore water pressure affected the factor of safety. This analysis was performed in three parts, holding two parameters constant at their average values and spanning the third over its full range. This was done using the R_u, friction angle, and cohesion values at ranges of 0 to 1, 10° to 16°, and 33 kPa to 63 kPa, respectively. While a R_u value of 0.5 typically indicates fully saturated conditions, we chose the upper value of 1 for this analysis due to the high pore water pressure found within FDL-A. Figure 3.14 is a graph of the sensitivity analysis results comparing the friction angle, cohesion, and R_u. The factor of safety is less sensitive to the friction angle than to cohesion, and it is affected most by variations in the pore water pressure. These higher sensitivities to cohesion and pore water pressure are significant factors if the movement of FDL-A is temperature-dependent. Considering the areas of massive ice observed, increases in temperature that cause melting of the ice will increase pore water pressure and potentially decrease the cohesive strength of the soil, both of which will lower the factor of safety significantly.

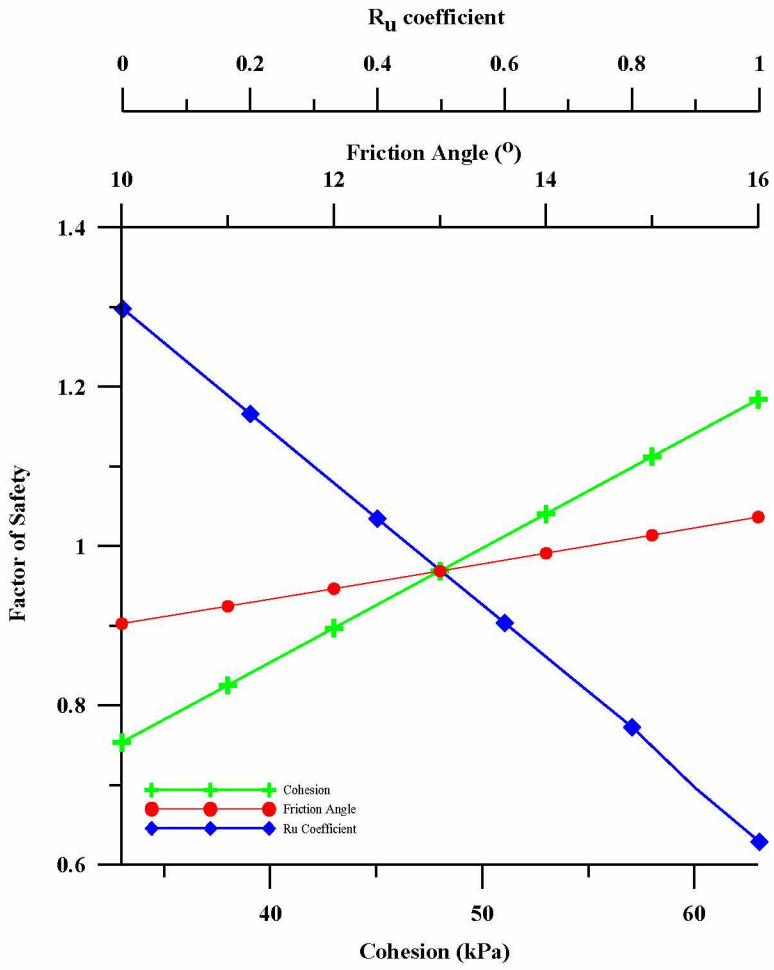

Figure 3.14. Sensitivity analysis results for friction angle, cohesion, and R_u coefficient.

CHAPTER 4 DISCUSSION

The U.S. National Climate Assessment (Chapin et al., 2014) reported that over the last 60 years, Alaska has warmed at more than twice the rate of the rest of the United States. Considering the temperature dependence of permafrost, impacts of this change have been evident throughout the region. There is a measured increase in permafrost temperatures which are projected to continue to rise (Smith et al., 2010) and models forecast that permafrost in Alaska will continue to thaw (Jafarov et al., 2012).

Our ongoing observations and analyses have shown that FDL-A is a dynamic feature. Both surface and subsurface measurements indicate that FDL-A's movement is temperature dependent and with current changes in Alaska's climate, this has significant implications for the nearby infrastructure. The slope stability analysis indicated a sensitivity of cohesion and pore water pressure on the lobe's factor of safety. As with any slope stability issue, water is an essential factor that cannot be ignored. This is especially true for FDL-A's current situation. The melting of massive ice (such as the infiltration ice exposed in RTSs) and thawing of frozen soil will increase pore water pressure and lower the soil's shear strength, resulting in the acceleration of FDL-A towards the Dalton Highway. While the results were instructive, our modeling efforts were constrained by lack of subsurface data. Additional drilling and/or investigation using geophysical methods will help to develop a more complete subsurface model. The traditional slope stability modeling also does not account for the soil strength's temperature dependency or phase change.

The purpose of the GIS analysis was to develop a tool for examining other FDLs along the Dalton Highway corridor; however, it also provided some insight into movement and areas of

instability on FDL-A. Through the slope analysis, we identified differential movement processes indicated by lobate step-like features on the lobe surface, recognizing one of the several movement processes that occur on FDL-A. Areas of low vegetation cover correlated well with field observations indicating highly active and unstable portions of the lobe. When additional high resolution imagery becomes available, this will be a valuable tool in recognizing surges of movement and active areas on other FDLs. A temporal analysis also can be performed to identify major changes in vegetation cover and actively moving areas on FDLs.

A statistical analysis of the catchment characteristics using GIS will be useful to determine similarities among FDLs. These characteristics include the catchment size, slope angle, aspect, rock type, and vegetation coverage. We also anticipate that such analysis will reveal common conditions contributing to lobe formation, as well as significant differences that explain the absence of lobes in adjacent catchments, resulting in a comprehensive hazard analysis for this area.

CHAPTER 5 CONCLUSION

FDL-A is an active frozen debris lobe in the south-central Brooks Range, Alaska. Its current location, just under 40 m upslope from the Dalton Highway, and increasing rate of movement pose a risk to infrastructure as debris may obstruct the highway and access to the Trans Alaska Pipeline System. FDL-A is mainly composed of silty sand and gravel, which is supplied to the lobe through solifluction and rock fall. Massive ice is present within the lobe in the form of infiltration ice, which forms as rain and some snow melt infiltrates and freezes within cracks open at the surface. Measurements indicate that FDL-A exhibits different mechanisms of movement with the majority of downslope movement occurring in a shear zone located 20.6 to 22.8 m bgs where measured. Another mechanism of movement is internal flow that is highly dependent on temperature. Surface measurements taken from October 2012 to March 2015 indicate an average rate of movement of 1.2 cm per day, which is an increase over historic rates and has the potential to increase further with climate projections pointing towards increasing temperatures in Alaska. As these features are found throughout the Dalton Highway corridor between MP 194 and MP 230, we developed a GIS protocol for the future analysis and comparison of multiple FDLs for an overall hazards assessment. The protocol includes examining catchment and lobe features such as: rock type, slope, aspect, and vegetation coverage.

The slope stability analysis performed on FDL-A required a back analysis to determine the soil strength parameters at failure, which resulted in significantly lower cohesion values, ranging from 43 to 53 kPa while maintaining friction angle values between 10° and 16°. When using these lower strength values, the analysis indicated a failure surface in a similar location as

to what we observed from our subsurface investigation. This analysis also indicated that the stability of FDL-A is highly sensitive to cohesion and pore water pressure.

This multi-faceted research has both increased our understanding of FDL-A and identified shortcomings in the available data sets and analysis techniques. A more in-depth slope stability analysis requires the development of a new modeling approach that incorporates the soil strength's temperature-dependency and phase change, and additional drilling and sampling and/or employing geophysical methods are essential for future modeling efforts. These additional field studies will help to define the pore water pressure distribution, locations of infiltration ice bodies, and multiple shear zones present within the lobe. Additional GIS analysis with high resolution data sets will help to determine historic rates of other FDLs identified for further study, thus providing a more comprehensive hazards analysis. Finally, we recommend continued surface movement measurements and field observations to document the dynamics of these mass movement features on permafrost-affected slopes.

REFERENCES

Alaska Earthquake Center, 2013, *AEIC Earthquake Database:* Electronic data available at http://www.aeic.alaska.edu/html_docs/db2catalog.html

ASTM, 1990, *D2216-90 Standard Test Methods for Laboratory Determination of Water (Moisture) Content of Soil and Rock by Mass:* ASTM International, West Conshohocken, PA, 7 p.

ASTM, 1990, *D3080-90 Standard Test Method for Direct Shear Test of Soils Under Consolidated Drained Conditions:* ASTM International, West Conshohocken, PA, 9 p.

Barboux, C.; Delaloye, R.; and Lambiel, C., 2014, Inventorying slope movements in an alpine environment using DInSAR: *Earth Surface Processes and Landforms,* Vol. 39, pp. 2057-2099.

Brown, J. and Kreig, R. A., 1983, *Guidebook to Permafrost and Related Features along the Elliott and Dalton Highways, Fox to Prudhoe Bay, Alaska:* Alaska Division of Geological and Geophysical Surveys Guidebook, 230 p.

Chapin, F. S., III, Trainor, S. F., Cochran, P., Huntington, H., Markon, C., McCammon, M., McGuire, A. D., and Serreze, M., 2014, Alaska. Climate Change Impacts in the United States. In Melillo, J. M., Richmond, T. C., and Yohe, G.W. (Editors), *The Third National Climate Assessment.* U.S. Global Change Research Program, pp. 514-536.

Daanen, R. P.; Grosse, G.; Darrow, M. M.; Hamilton, T. D.; and Jones, B. M., 2012, Rapid movement of frozen debris-lobes: implications for permafrost degradation and slope instability in the south-central Brooks Range, Alaska: *Natural Hazards and Earth System Science:* Vol. 12, pp. 1521-1537.

Darrow, M. M., Daanen, R. P., and Simpson, J. M., 2013, Analysis of a frozen debris lobe: a first look inside an impending geohazard. *ISCORD 2013:* pp. 139-148.

Darrow, M. M., Simpson, J. M., Daanen, R. P., and Hubbard, T., 2015, Characterizing a frozen debris lobe, Dalton Highway, Alaska. *ASCE Cold Regions Engineering Conference:* (in press).

Davis, N., 2001, *Permafrost: A Guide to Frozen Ground in Transition:* University of Alaska Press, Fairbanks, AK, 351p.

Dillon, J. T.; Harris, A. G.; Dutro, Jr., J. T.; Solie, D. N.; Blum, J.D.; Jones, D. L.; and Howell, D. G., 1988, *Preliminary Geologic Map and Section of the Chandalar D-6 and Parts of the Chandalar C-6 and Wiseman C-1 and D-1 Quadrangles, Alaska:* Alaska Division of Geological and Geophysical Surveys Report of Investigation 88-5, scale 1:63,360.

Douglas, T. A.; Fortier, D.; Shur, Y. L.; Kanevskiy, M. Z.; Guo, L.; Cai, Y.; and Bray, M. T., 2011, Biogeochemical and geocryological characteristics of wedge and thermokarst-cave ice in the CRREL permafrost tunnel, Alaska: *Permafrost and Periglacial Processes*, Vol. 22, pp. 120-128.

Duncan, J. M., 1996, Soil Slope Stability Analysis. In *Landslides: Investigation and Mitigation,* Transportation Research Record 247, National Research Council, Washington D.C., pp. 337-371.

Esri, 2015, *ArcGIS World Imagery:* Electronic data available at http://goto.arcgisonline.com/maps/world_imagery

Geographic Information Network of Alaska (GINA), 2001, *Interferometric Synthetic Aperature Radar (IfSAR).*

GEO-SLOPE International Ltd., 2008, *Stability Modeling with SLOPE/W 2007; An Engineering Methodology:* 4th Ed., Alberta, Canada, 355 p.

Gonzalez de Vallejo, L. I. and Ferrer, M., 2011, *Geological Engineering:* CRC Press, New York, NY, 678 p.

Haeberli, W. and Beniston, M., 1998, Climate change and its impacts on glaciers and permafrost in the Alps: *Ambio,* Vol. 27, No. 4, pp. 258-265.

Haeberli, W.; Hallet, B.; Arenson, L.; Elconin, R.; Humlum, O.; Kääb, A.; Kaufman, V.; Branko, L.; Matsuoka, N.; Springman, S.; and Vonder Mühll, D., 2006, Permafrost creep and rock glacier dynamics: *Permafrost and Periglacial Processes,* Vol. 17, pp. 189-214.

Hamilton, T. D., 1978, *Surficial Geologic Map of the Chandalar Quadrangle, Alaska:* U.S. Geological Survey Miscellaneous Field Studies Map MF-878A, scale 1:250,000.

Hamilton, T. D., 1979, *Surficial Geologic Map of the Wiseman Quadrangle, Alaska:* U.S. Geological Survey Miscellaneous Field Studies Map MF-1122, scale 1:250,000.

Hamilton, T. D., 1981, *Surficial Geologic Map of the Survey Pass Quadrangle, Alaska:* U.S. Geological Survey Miscellaneous Field Studies Map MF-1320, scale 1:250,000.

Harris, C., 2005, Climate change, mountain permafrost degradation and geotechnical hazard: *Global Change and Mountain Regions,* pp. 215-224.

Harris, C.; Aaronson, L. U.; Christiansen, H. H.; Etzemüller, B.; Frauenfelder, R.; Gruber, S.; Haeberli. W.; Hauck, C.; Hölzle, M.; Humlum, O.; Isaksen, K.; Kääb, A.; Kern-Lütschg, M. A.; Lehning, M.; Matsuoka, N.; Murton, J. B.; Nötzli, J.; Phillips, M.; Ross, N.; Seppälä, M.; Springman, S. M.; and Vonder Mühll, D., 2009, Permafrost and climate in Europe: Monitoring and modeling thermal, geomorphological and geotechnical responses: *Earth-Science Reviews,* Vol. 92, pp. 117-171.

Harris, C.; Davies, M. C.; and Etzelmüller, B., 2001, The assessment of potential geotechnical hazards associated with mountain permafrost in a warming global climate: *Permafrost and Periglacial Processes,* Vol. 12, pp. 145-156.

Harris, C. and Lewkowicz, A. G., 2000, An analysis of the stability of thawing slopes, Ellesmere Island, Nunavut, Canada: *Canadian Geotechnical Journal,* Vol. 37, pp. 449-462.

Harris, C. and Vonder Mühll, D., 2001, Permafrost and climate in Europe. Climate change, mountain permafrost degradation and geotechnical hazard: *Global Change and Protected Areas,* pp. 71-82.

Hubbard, T. D.; Koehler, R. D.; and Combellick, R. A., 2011, *High-resolution lidar data for Alaska infrastructure corridors.* Lidar Datasets of Alaska: Alaska Division of Geological and Geophysical Surveys Raw Data File 2011-3, 291 p.

Hubbard, T. D., Spangler, E. R., Daanen, R. P., Darrow, M. M., Simpson, J. M., and Southerland, L. E., 2013, Frozen debris lobes- Characterizing a potential geologic hazard along the Dalton Highway, southern Brooks Range, Alaska (poster): G*eological Society of America Annual Meeting, Denver, Colorado, October 27, 2013, Abstracts with Programs,* Vol. 45, No.7, p. 152: Alaska Division of Geological and Geophysical Surveys, 1 sheet. doi: 10.14509/29133

Huscroft, C. A.; Lipovsky, P.; and Bond, J. D.; 2003, Permafrost and landslide activity: Case studies from southwestern Yukon Territory. In Emond, D. S. and Lewis, L. L. (Editors), *Yukon Exploration and Geology.* Yukon Geological Survey, pp. 107-119.

Jafarov, E. E.; Marchenko, S. S.; and Romanovsky, V. E.; 2012, Numerical modeling of permafrost dynamics in Alaska using a high spatial resolution dataset: *The Cryosphere,* Vol. 6, pp. 613-624.

Kääb, A.; Reynolds, J. M.; and Haeberli, W.; 2005, Glacier and permafrost hazards in high mountains: *Global Change and Mountain Regions,* pp. 225-234.

Kreig, R. A. and Reger, R. D., 1982, *Air-photo Analysis and Summary of Landform Soil Properties along the Route of the Trans-Alaska Pipeline System:* Alaska Division of Geological and Geophysical Surveys, Anchorage, Alaska.

Lipovsky, P. and Huscroft, C. A., 2006, A reconnaissance inventory of permafrost-related landslides in the Pelly River watershed, central Yukon. In Emond, D. S., Lewis, L. L., and Weston, L.H. (Editors), *Yukon Exploration and Geology.* Yukon Geological Survey, pp. 181-195.

Lyle, R. and Hutchinson, D. J., 2006, Influence of degrading permafrost on landsliding processes: Little Salmon Lake, Yukon Territory, Canada: *Geohazards; Engineering Conferences International,* 11 p.

Matsuoka, N., 2001, Solifluction rates, processes and landforms: a global review: *Earth-Science Reviews,* Vol. 55, pp. 107-134.

Matsuoka, N., 2014, Combining time-lapse photography and multisensor monitoring to understand frost creep dynamics in the Japanese Alps: *Permafrost and Periglacial Processes,* Vol. 25, pp. 94-106.

Meyer, H.; Dereviagin, A.; Siegert, C.; Schirrmeister, L.; and Hubberten, H.-W., 2002, Palaeoclimate reconstruction on Big Lyakhovsky Island, North Siberia – hydrogen and oxygen isotopes in ice wedges: *Permafrost and Periglacial Processes*, Vol. 13, pp. 91-105.

Meyer, H.; Schirrmeister, L.; Andreev, A.; Wagner, D.; Hubberten, H.-W.; Yoshikawa, K.; Bobrov, A.; Wetterich, S.; Opel, T.; Kandiano, E.; and Brown, J., 2010, Lateglacial and Holocene isotopic and environmental history of northern coastal Alaska – results from a buried ice-wedge system at Barrow: *Quaternary Science Reviews*, Vol. 29, pp. 3720-3735.

Mull, C. G. and Adams, K.E. (Editors), 1989, *Bedrock Geology of the Eastern Koyukuk Basin, central Brooks Range, and east-central Arctic Slope along the Dalton Highway, Yukon River to Prudhoe Bay, Alaska, Volume 1:* Alaska Division of Geological and Geophysical Surveys Guidebook 7, Vol. 1, 309 p.

Scher, R. L., 1996, Geotechnical Considerations. In *Cold Regions Utilities Monograph,* 3rd Ed, American Society of Civil Engineers, pp 3.1-3.115.

Smith, S. L.; Romanovsky, V. E.; Lewkowicz, A. G.; Burn, C. R.; Allard, M.; Clow, G.D.; Yoshikawa, K.; and Throop, J., 2010, Thermal state of permafrost in North America: a contribution to the International Polar Year: *Permafrost and Periglacial Processes,* Vol. 21, pp. 117-135.

Spangler, E., Hubbard, T. D., Daanen, R. P., Darrow, M. M., Simpson, J. M., and Southerland, L., 2013, Geological and geomorphic characterization of frozen debris lobe catchments along the Dalton Highway, southern Brooks Range, Alaska (poster): *Geological Society of America Annual Meeting, Denver, Colorado, October 27, 2013, Abstracts with Programs*, V. 45, No. 7, p. 152: Alaska Division of Geological & Geophysical Surveys, 1 sheet. doi:10.14509/27007

Spangler, E. R. and Hubbard, T. D., in review, *Geologic and geomorphic characterization of frozen debris lobe source basins along the Dalton Highway, southern Brooks Range, Alaska:* Alaska Division of Geological and Geophysical Surveys.

Tart Jr., R. G., 1996, Permafrost. In *Landslides: Investigation and Mitigation,* Transportation Research Record 247, National Research Council, Washington D.C., pp. 620-643.

Tarussov, A., 1992, The Arctic from Svalbard to Severnaya Zemlya: climatic reconstructions from ice cores. In Bradley, R. S., and Jones, P. D. (Editors), *Climate Since A.D. 1500*, Routledge, pp. 505-516.

Tsytovich, N. A., 1975, *The Mechanics of Frozen Ground:* Scripta Book Company, Washington D.C., 426 p.

Vyalov, S. S., 1986, *Rheological Fundamentals of Soil Mechanics: Development in Geotechnical Engineering,* Vol 36: Elsevier Science Publishing Company, Inc., New York, NY, 564 p.

Wahrhaftig, C. and Cox, A., 1959, Rock glaciers in the Alaska Range: *Bulletin of the Geological Society of America,* Vol. 70, No. 4, pp. 383-436.

Washburn, A. L., 1985, Periglacial problems. In Church, M. and Slaymaker, O. (Editors), *Field and Theory: Lectures in Geocryology*: University of British Columbia Press, pp. 166-202.

Wesson, R. L., Boyd, O. S., Mueller, C. S., Bufe, C. G., Frankel, A. D., Petersen, M. d., 2007, *Revision of Time-Independent Probabilistic Seismic Hazard Maps for Alaska:* U.S. Geological Survey Open-File Report 2007-1043, 33 p.

Williams, P. J. and Smith, M. W., 1989, *The Frozen Earth: Fundamentals of Geocryology*: Cambridge University Press, 306 p.

APPENDIX A SOIL CLASSIFICATION RESULTS FOR ALL INVESTIGATED FROZEN DEBRIS LOBES (FDLS)

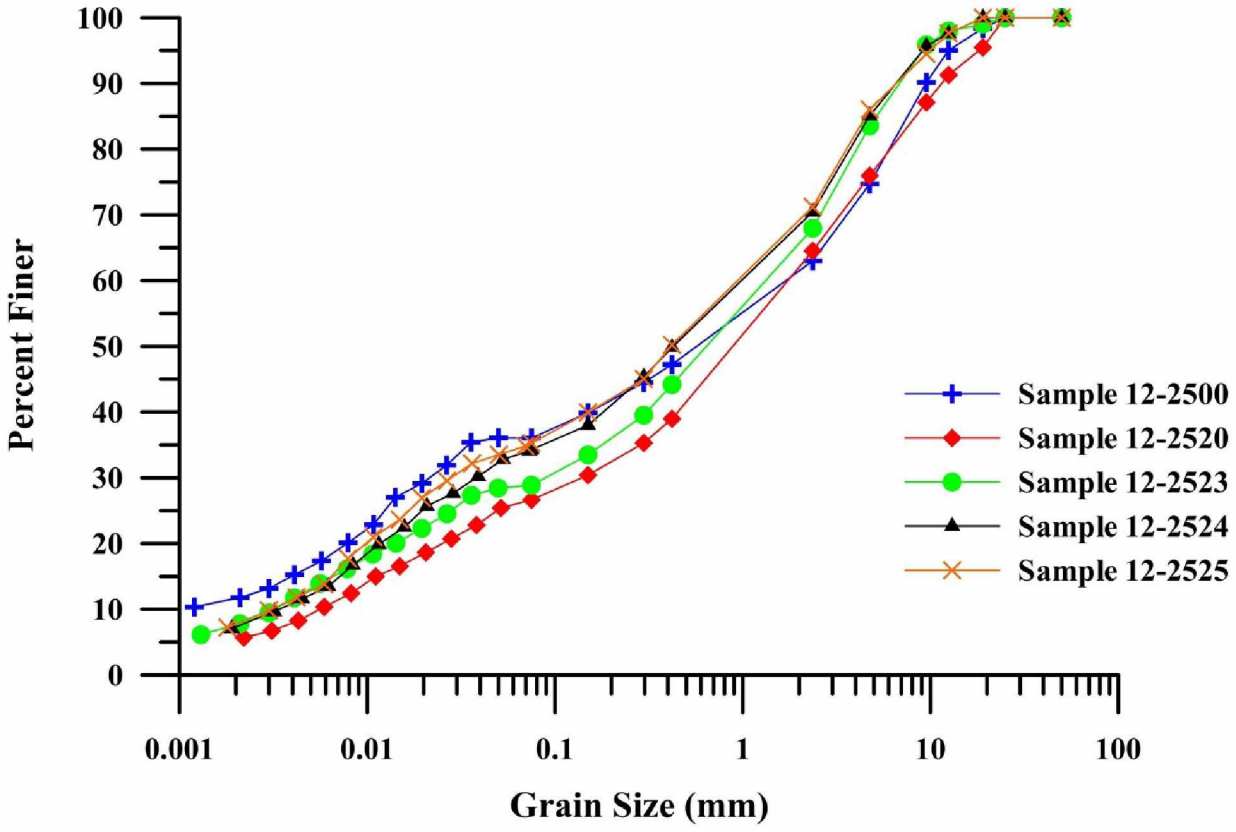

Figure A.1. Grain size analysis results for FDL-A.

Table A.1. USCS soil classifications for FDL-A.

Sample	Classification
12-2500	Silty sand with Gravel (SM)
12-2520	Silty sand with Gravel (SM)
12-2523	Silty sand with Gravel (SM)
12-2524	Silty sand (SM)
12-2525	Silty sand (SM)

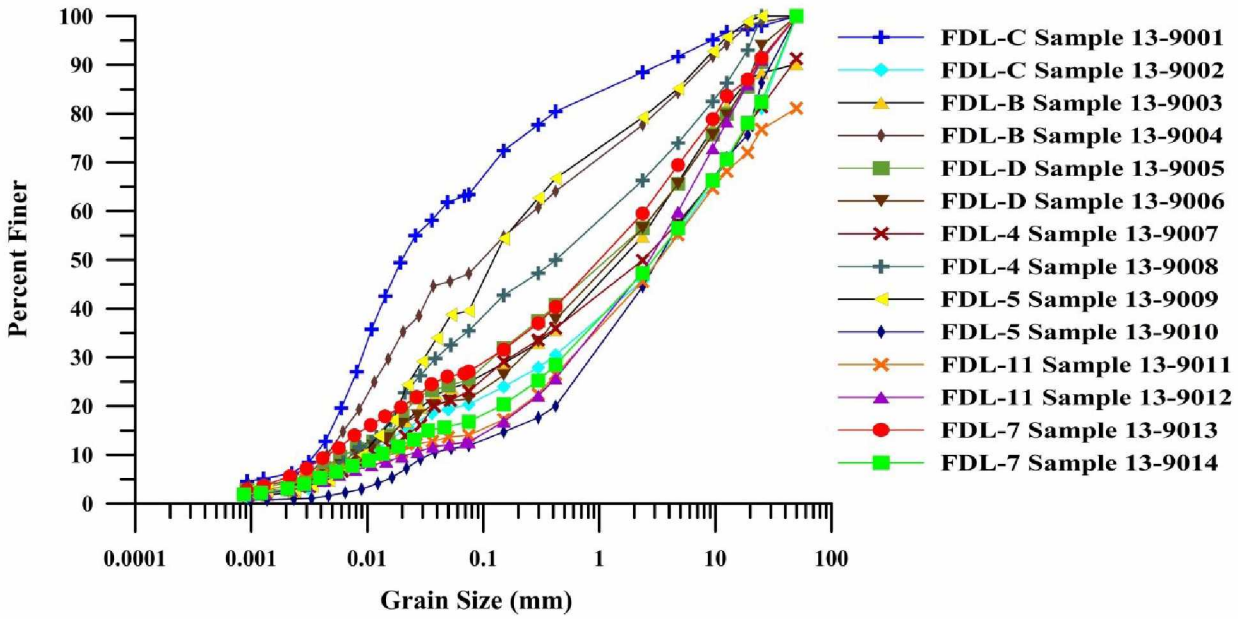

Figure A.2. Grain size analysis results for the additional seven FDLs investigated.

Table A.2. USCS soil classifications for the additional seven FDLs investigated.

FDL	Sample	Classification
FDL-C	13-9001	Sandy silt (w/ high organics), ML
FDL-C	13-9002	Silty gravel with Sand, GM
FDL-B	13-9003	Silty sand with Gravel, SM
FDL-B	13-9004	Silty sand with Gravel, SM
FDL-D	13-9005	Silty sand with Gravel, SM
FDL-D	13-9006	Silty sand with Gravel, SM
FDL-4	13-9007	Silty gravel with Sand, GM
FDL-4	13-9008	Silty sand with Gravel, SM
FDL-5	13-9009	Silty sand, SM
FDL-5	13-9010	Poorly graded sand with Silt and Gravel, SP-SM
FDL-11	13-9011	Silty gravel with Sand, GM
FDL-11	13-9012	Silty sand with Gravel, SM
FDL-7	13-9013	Silty sand with Gravel, SM
FDL-7	13-9014	Silty gravel with Sand, GM

APPENDIX B POINT LOAD INDEX TEST RESULTS OF UNIAXIAL COMPRESSIVE STRENGTH FOR FDL ROCK SAMPLES

Table B.1. Point load index test results for FDL rock samples. Samples collected from FDL catchment areas. The symbol 'σ_c' represents uniaxial compressive strength. (Descriptions by T. Hubbard).

Sample	Rock Type and Description	FDL	σ_c (MPa)
102	Phyllite: green weathering; sandy texture in places; foliated	FDL 7	26.17
103	Limestone, mixed with phyllite: blocky; competent	FDL 7	60.72
105	Schist: foliated; boudins	FDL 7	42.23
106	Phyllite: platy; foliated	FDL 11	52.75
107	Phyllite: platy; mm-scale foliations; occasionally sandy	FDL 11	40.31
108	Phyllite/Gneiss: higher specific gravity; bands ~1-mm thick	FDL 4	34.58
109	Phyllite/Gneiss: higher specific gravity; bands ~1-mm thick; caliche	FDL 4	26.25
110	Phyllite/Gneiss: higher specific gravity; bands ~1-3-mm thick; micaceous	FDL 5	29.83
111	Phyllite: thinly foliated (1-3 mm); possibly graphitic? white mica?	FDL 5	14.00
112	Metasandstone: in places looks like a phyllite; gray; brown weathering; fine sand texture; folded; calcareous	FDL B	50.40
113	Metasandstone: in places looks like a phyllite; 4-5-cm wide plates; foliated	FDL B	77.32
116	Limestone: massive; calcareous; caliche; sugary or sandy texture	FDL D	34.33
117	Phyllite or metasiltstone: foliated; platy; silt texture	FDL D	32.85

Table B.1 (continued). Point load index test results for FDL rock samples. Samples collected from FDL catchment areas. The symbol 'σ_c' represents uniaxial compressive strength. (Descriptions by T. Hubbard).

Sample	Rock Type and Description	FDL	σ_c (MPa)
118	Skarn: crystalline; somewhat foliated; inclusions?	FDL D	25.73
119	Gabbro: crystalline; slightly foliated? plagioclase feldspar? horneblende?	FDL D	15.22
121	Phylllite: finely foliated (1-2 mm); silt to clay texture	FDL D	20.60
122	Limestone: massive to weakly foliated; some caliche; sandy texture	FDL D	45.78